Published in : Carbohydrate Polymers (2020), vol. 230, 115634
DOI: 10.1016/j.carbpol.2019.115634
Status : Postprint (Author's version)

ALDEHYDE-CONJUGATED CHITOSAN-GRAPHENE OXIDE GLUCODYNAMERS: TERNARY COOPERATIVE ASSEMBLY AND CONTROLLED CHEMICAL RELEASE

Jamal Chabbi[a,b,c], Abdelhafid Aqil[b], Nadia Katir[a], Bénédicte Vertruyen[b], Christine Jerôme[b], Mohamed Lahcini[c,d], Abdelkrim El Kadib[a,*]

[a] *Euromed Research Center. Engineering Division, Euro-Med University of Fes (UEMF), Route de Meknes, Rond-point de Bensouda. 30070 Fès, Morocco*

[b] *Centre for Education and Research on Macromolecules, CESAM Research Unit, Chemistry Department, University of Liege, Sart-Tilman B6a, Allée de la Chimie 4000 Liège, Belgium*

[c] *Laboratory of Organometallic and Macromolecular Chemistry-Composites Materials, Faculty of Sciences and Technologies, Cadi Ayyad University, Avenue Abdelkrim Elkhattabi, B.P. 549, 40000 Marrakech, Morocco*

[d] *Mohammed VI Polytechnic University, Lot 660, Hay Moulay Rachid, 43150 Ben Guerir, Morocco*

Keywords :
Chitosan, Graphene oxide, Aldehyde-functionalization, Nanostructured films, Chemical release

Abstract

Simultaneous condensation of aromatic aldehydes (**Ar_xCHO**; *x* = 1–4) on chitosan biopolymer (**CS**) affords, after water-evaporation, structurally-conjugated aryl-functionalized **CS-Ar_x-*f*** films. Similarly, cooperative assembly of two-dimensional nanometric graphene oxide (**GO**), aromatic aldehyde and chitosan provides transparent, flexible and crack-free aldehyde-functionalized, ternary-reinforced **CS-Ar_x-GO-*f*** nanocomposite films. Homogenous films were obtained using *ortho*-hydroxybenzaldehyde **Ar_1** while the *para*-hydroxybenzaldehyde **Ar_4** was prone to packing inside. Textural and mechanical properties were investigated and expectedly, significant improvement was found for **CS-Ar_1-GO-*f*** because of the great dispersion of the aromatic and the presence of the filler. The sensitivity of unsaturated C=N imine bond to hydrolysis was explored for triggering controlled release of aromatics from the as-prepared films. All of them were found to induce a time-dependent aromatic release. It has been moreover observed that the release was significantly delayed in **CS-Ar_x-GO-*f*** compared to **CS-Ar_x-*f***, a fact attributed to the interplay of the ring with the basal and edges of graphene oxide, through π-π stacking and additional hydrogen bonding interactions. This finding shows that beyond the conventional wisdom using fillers for improving thermal and mechanical properties, the tiny carbon sheets can act as a regulator for aldehyde release, thereby providing a way for more controlled chemical delivery from confined nanocomposites.

Published in : Carbohydrate Polymers (2020), vol. 230, 115634
DOI: 10.1016/j.carbpol.2019.115634
Status : Postprint (Author's version)

1. Introduction

Chitosan (CS) is one of the most interesting biomass-waste with its starting acetylated chitin source being ranked as the second most abundant polysaccharide after cellulose (Rinaudo, 2006). The particularism of this nitrogen-containing carbohydrate copolymer can be rooted in the presence of primary amine (NH_2) in the main chain backbone. This pH-sensitive group allows for regulating chitosan physical-chemical properties, electrolytic and amphiphilic behavior and is at the basis of its gelation ability to provide cross-linked hydrogels and self-standing porous microspheres (El Kadib & Bousmina, 2012; El Kadib, Bousmina, & Brunel, 2014; Yi et al., 2005). The presence of highly-reactive nitrogen-containing groups provides a handle to trivial conjugation of a large diversity of functional chemicals on the biopolymer skeletal (*via* Schiff base formation, peptide coupling, cationic exchange, *etc*.) (Macquarrie & Hardy, 2005; Thakur & Thakur, 2014). This allowed the implementation of chitosan in diverse applications including carrier systems for sustained release of active ingredients, biodegradable films for food-packaging and biomedical use, water treatment for removal of heavy metals and organic pollutants, reactive membranes for micro- and nano-filtration, catalysis, etc (Croisier & Jérôme, 2013; El Kadib, 2015; Rabea, Badawy, Stevens, Smagghe, & Steurbaut, 2003; Sahariah & Másson, 2017; Suginta, Khunkaewla, & Schulte, 2013; Wang, Qian, & Ding, 2018).

One of the most exciting features of chitosan lies in the possibility to transform its aqueous colloidal solution to nanostructured films (Hammi et al., 2019; Ladet, David, & Domard, 2008; Pavinatto, Caseli, & Oliveira, 2010). Unfortunately, native chitosan films display moderate thermal and chemical stability and cannot often withstand the requested conditions of practical handling. Consequently, their suitability for realistic applications depends to a large extent on the improvement of their thermal, chemical and mechanical stability. Common way to improve the above mentioned properties uses nanometric fillers, among which graphene demonstrated already its efficiency (Alcântara, Darder, Aranda, & Ruiz-Hitzky, 2014; Anouar et al., 2019; Darder, Colilla, & Ruiz-Hitzky, 2003, 2006; Ennajih, Bouhfid, Essassi, Bousmina, & El Kadib, 2012; Frindy et al., 2016; Jović-Jovičić et al., 2016; Purwanto et al., 2016). Beyond the improvement in their mechanical properties, the use of graphene as filler provides additional benefits for these nanocomposites including electronic properties, conductivity, light-weight and hydrophobicity, thereby opening new opportunities in wearable electronic technologies (Frindy et al., 2017; Han, Yan, Chen, & Li, 2011; Yang, Tu, Li, Shang, & Tao, 2010).

A scalable approach to graphene derivatives consists on the liquid-phase assisted oxidation of graphite followed by sonication to provide graphene oxide (**GO**) sheets (Hummers & Offeman, 1958). The resulting **GO** displays strong interfacial properties that allows efficient manufacturing of nanocomposites without the need for compatibilizers or harsh treatment conditions (He, Wang, Xia, Sun, & Song, 2014; Pan, Wu, Bao, & Li, 2011).

While the association of chitosan with clay or carbon nanoparticles is a well-known strategy, (Darder et al., 2003; Ennajih et al., 2012; Frindy et al., 2016, 2017), no report has investigated the preparation of a ternary nanocomposite based on chitosan, filler nanoparticle and reactive aldehyde. Such unknown functional nanocomposites, different from those entrapping active ingredients, can offer

Published in : Carbohydrate Polymers (2020), vol. 230, 115634
DOI: 10.1016/j.carbpol.2019.115634
Status : Postprint (Author's version)

more control for the progressive release of fertilizers in agriculture and the delivery of pharmaceutical ingredients in nanomedicine. Besides, chitosan is fully degradable and its utilization will avoid the generation of persisting microplastics from petroleum-based polymer nanocomposites.

In 2012, Marin and Barbiou reported that the yield of amine-to-aldehyde condensation can be significantly improved during solvent evaporation in hydrogels and films (Marin, Ailincai, Morariu, & TartauMititelu, 2017; Marin, Simionescu, & Barboiu, 2012, 2013; Marin et al., 2014, 2015). Following this breakthrough, we have succeeded in preparing a set of transparent and flexible aromatic-functionalized chitosan-montmorillonite films (denoted as **CS-Ar$_x$-MMT-*f***) (Chabbi et al., 2018). Because the biopolymer and the starting aromatic aldehyde are covalently linked through C=N bonding (Antony, Arun, & Manickam, 2019; Godoy-Alcántar, Yatsimirsky, & Lehn, 2005; Schiff, 1864) and that the latter can be cleaved in water medium (Dohno, Okamoto, & Saito, 2005), we triggered the release of the aromatics from the films upon water exposure. Unexpectedly, we unveiled a pivotal role of the filler polarity during C]N hydrolysis, allowing for discriminative release of chemicals from these biodegradable films (Chabbi et al., 2018). These results prompted us to investigate the incorporation of other fillers in analogues functionalized chitosan films. Considering that the basal graphene sheet is rather hydrophobic, we reasonably expected different scenarios in chitosan-graphene oxide films compared to the fully hydrophilic chitosan-montmorillonite (different materials properties, different host-guest interaction types, different resistivity to the medium…). Moreover, graphene oxide is a much more suitable filler to improve the chemical stability of chitosan, and in such a way, chemical release will not interfere with the polysaccharide degradability (Frindy et al., 2017).

We herein describe the ternary cooperative assembly of aromatic aldehyde, chitosan biopolymer and graphene oxide to access nanostructured aldehyde-functionalized chitosan-graphene oxide gluco-dynamers. Four aromatic aldehydes with different substituents position were selected for this study. Ternary **CS-Ar$_x$-GO-*f*** nanocomposites were prepared by mixing the three components followed by water-evaporation and film casting. Native, non-modified chitosan film labelled as **CS-*f*** and **CS-Ar$_x$-*f*** (without graphene oxide) were also prepared for comparison. Insight was gained on their chemical composition, textural properties and surface features by diffuse reflectance infrared spectroscopy (DRIFT) and diffuse reflectance UV–vis spectroscopy (DRUV) analyses, X-ray diffraction (XRD), scanning and transmission electronic microscopy (SEM and TEM) and contact angle measurements. Thermal properties were also investigated by TGA and DSC analyses. Variation on their mechanical properties was assessed depending on the nature of conjugated aromatics and the presence or not of graphene oxide fillers. Lastly, controlled-release of the aromatics from the transparent films was triggered under different conditions (pH, temperature, time) to assess their suitability as biodynamic drug-delivery films (see the experimental part for more details).

2. Experimental section

2.1. MATERIALS

Chitosan (CS) with degree of deacetylation of ~ 90 % (as calculated by FTIR analyses) was purchased from Sigma Aldrich, in powder from, with high viscosity and an average molecular weight of 200–800

Published in : Carbohydrate Polymers (2020), vol. 230, 115634
DOI: 10.1016/j.carbpol.2019.115634
Status : Postprint (Author's version)

cps. Graphene oxide (**GO**) was obtained by oxidation of graphite flakes using modified hummers method (Hummers & Offeman, 1958). Salicylaldehyde (**Ar_1CHO**), 5-bromosalicylaldehyde (**Ar_2CHO**), 3,5-dimethoxybenzaldehyde (**Ar_3CHO**), 4-hydroxybenzaldehyde (**Ar_4CHO**) and all other reagents (ethanol, tetrahydrofuran and acetic acid) were obtained from Sigma Aldrich with analytical grades and used without further purification.

2.2. GENERAL

The Fourier transform infrared (Thermo Scientific iD5 Diamond ART for Nicolet iS5 FT-IR Spectrometer) spectra of films in the range, from 400 to 4000 cm^{-1}, with a resolution of 1 cm^{-1}. X-ray diffraction (diffractometer D8 Advance type Bruker) was used with Cu Kα radiation at room temperature. Deeper surface morphology study was performed using field emission electron microscopy (XL 30 FEG-ESEM, FEI). The microscope was coupled to a dispersive energy spectrometer (EDX), which is an x-ray technique used to identify the elemental composition of chitosan films. Transmission Electron Microscopy was performed with Philips/FEI CM100 at room temperature. Surface wettability of the films was assessed through contact angle measurement (Digidrop, DGD, Fast 60, Contact Angle Meter, GBX) at room temperature. The cutted film (3 cm x 3 cm) was fixed on the top of a dynamic support. Droplet (3 µL) was placed on the film surface and the change of contact angles was treated by the software of the machine. Each measurement was repeated four times and their average is considered. UV-visible spectroscopy was performed with UV-3100 instrument (1 nm of resolution from 200 to 300 nm, and an interval of 0.2 nm). Samples were prepared by immersing films in distilled water and monitoring of release as a function of three parameters: time, temperature and pH. Each measurement is repeated three times (3 different samples) and their average is considered. TGA analysis was carried out on a TGA Q500. The samples were measured with 10 °C/min over the temperature range of 20–700 °C under nitrogen atmosphere. Approximately 5 mg of samples were cut from the films for this analysis. Differential Scanning Calorimetry (DSC) thermograms are measured using a differential scanning calorimeter (model Q100 from TA instruments). Samples of 5–10 mg were accurately weighed and placed in aluminum DSC pans. The profile was obtained at a heating rate of 10 °C/min and scanning from 25 °C to 300 °C under nitrogen atmosphere. Mechanical properties were measured under dried conditions. The tensile strength and elongation of chitosan modified films were measured on a testing machine (Instron 5566, USA). The test involves putting a sample, 1 cm of width and 3 cm of length, between tow clamps stretched until getting the film ruptures. The results are the average of four independent measurements.

2.3. PREPARATION OF ALDEHYDE-FUNCTIONALIZED FILMS

Aqueous chitosan solution was prepared by dissolving 0.15 g of chitosan powder in 1.5 % (v/v) of acetic acid solution under magnetic stirring at 60 °C. The dissolution of chitosan took 3 h. Then, a well-defined amount of **Ar_xCHO** was introduced (**Ar_1CHO**: (109.9 mg, 0.9 mmol); **Ar_2CHO**: (180.9 mg, 0.9 mmol) in 10 ml of THF; **Ar_3CHO**: (149.6 mg, 0.9 mmol) in 10 ml of methanol; **Ar_4CHO**: (109.9 mg, 0.9 mmol) in 10 ml of ethanol) followed by stirring at 60 °C for two hours. The choice of the solvent was dictated by solubility reasons and no influence on the film quality was observed for native chitosan films prepared using the similar ratio of water: solvent. Graphene oxide suspension (3 wt%) previously treated under

Published in : Carbohydrate Polymers (2020), vol. 230, 115634
DOI: 10.1016/j.carbpol.2019.115634
Status : Postprint (Author's version)

ultrasonic waves was slowly added to the chitosan/aldehyde solutions to ensure good dispersion of the graphene oxide in the solution and the mixture was left for stirring for 2 additional hours. The suspension was then poured into petri dishes. The resulting casted film was removed, immersed in DMF solution (20 mL) for 3 or 4 min in order to remove adsorbed species and probable impurities existing on the surface of the films.

2.4. RELEASES STUDY OF ALDEHYDES IN WATER BY UV

The release of grafted aldehydes on chitosan film and reinforced by the graphene oxide is done by monitoring release of the aldehydes depending on pH, temperature and time in aqueous media. The release study of the aldehyde is done by the following experimental protocol: In 200 ml beaker containing a magnetic bar, 100 ml of distilled water was introduced. Then, 120 mg of aldehyde-functionalized chitosan film was added. The first contact between the film of chitosan and distilled water shows a value 4.5 of pH, which is associated with the presence of acetic acid in the film. pH was adjusted with NaOH solution. The amount of release aldehyde was determined by sampling 5 ml of the solution at different times, pH or temperatures. The times we have chosen for various samples are 1, 2, 3, 4, 5, 6 and 7 h. The temperature variation is set between 25 °C and 80 °C. The resulting solution was investigated by UV–vis spectroscopy to measure the concentration of the released aromatic. Before this, a calibration curve was determined for the four aldehydes with well-calculated amount of the aromatics. Plotting the value of the absorbance in the curve affords directly the corresponding concentration (Beer Lambert Equation).

3. Results and discussion

Fig. 1 illustrates the preparation of high-quality crack-free aldehyde-functionalized chitosan-graphene oxide films where chitosan, 3 wt % graphene oxide and four aromatic aldehydes were selected. Native chitosan film, denoted as **CS-*f*** and the newly prepared **CS-Ar$_x$-GO-*f*** were shown in the photos (**Fig. 1**).

3.1. CHEMICAL COMPOSITION AND STRUCTURAL ORGANIZATION OF ALDEHYDE-FUNCTIONALIZED FILMS

Structural alteration of the chitosan backbone with either aromatic aldehyde or graphene oxide or both of them was investigated by DRIFT analysis (**Figs. 2** and **S1** in Sup info). Native **CS-*f*** film reveals typical signals of chitosan where the vibration at 1022, 1330, 1551, 1641 and 3362 cm^{-1} are attributed to C—O—C, C—N, N—H, NHCO and —OH, respectively (Valentin, Bonelli, Garrone, Di Renzo, & Quignard, 2007). Comparatively, the significant decrease in NH_2 intensity at 1551 cm^{-1} and the complete disappearance of aldehyde signatures at 1700–1740 cm^{-1} in **CS-Ar$_x$-*f*** points to the occurrence of chemical condensation between primary amine of chitosan and aromatic aldehydes and ruled out the entrapment of the latter on the carbohydrate network via physical interactions (Ailincai, Bejan, Titorencu, Drobota, & Simionescu, 2014; Chabbi et al., 2018; Iftime, Morariu, & Marin, 2017; Marin et al., 2015; Olaru et al., 2018). The appearance of a novel bond between 1600 and 1640 cm^{-1}, assignable to the newly created C=N imine bond corroborates the chemical condensation of the primary amine of

Published in : Carbohydrate Polymers (2020), vol. 230, 115634
DOI: 10.1016/j.carbpol.2019.115634
Status : Postprint (Author's version)

chitosan to aromatic aldehydes (Ailincai et al., 2014; Chabbi et al., 2018; Iftime et al., 2017; Marin et al., 2015; Olaru et al., 2018). A slight shift was observed in C=N resonance (ν = 1604 cm^{-1}) of **CS-Ar$_4$-*f*** compared to the vibration observed at 1643 cm^{-1} for **CS-Ar$_1$-*f***, **CS-Ar$_2$-*f*** and **CS-Ar$_3$-*f***. **Ar$_4$CHO** features hydroxyl group in *para*-position with respect to aldehyde, which makes it more prone to interact, through hydrogen bonding, with alcohol groups of the adjacent fibers upon aryl condensation. Additional band assigned to unsaturated C]C bond of the benzene ring was observed at 1500 cm^{-1}, which further confirm the presence of the latter in the carbohydrate network (Ailincai et al., 2016; Stroescu et al., 2015).

In **CS-GO-*f***, the signature of chitosan was recognized but no significant shift was observed to probe its interaction with oxygenated groups of graphene oxide. Precedently, it has been reported that chitosan interacts with graphene oxide through multiple sites including ring opening of the epoxide by amine and hydrogen bonding between NH_2 and OH of chitosan with COOH and OH of graphene oxide (Frindy et al., 2017; Yang et al., 2010). The lower amount of graphene oxide (3 wt%) can probably explain the absence of significant shifting in **CS-GO-*f***. In the ternary **CS-Ar$_x$-GO-*f***, a complete disappearance of the aldehyde signature was observed concomitantly with a decrease of amine intensity and the appearance of new C=N bands. This variation confirms the occurrence of chemical conjugation between chitosan and aromatic aldehydes while graphene oxide serves for physical cross-linking of the carbohydrate network (Frindy et al., 2017). Interestingly, significant shift in C=N resonance was observed for **CS-Ar$_x$-GO-*f*** compared to graphene-free **CS-Ar$_x$-*f***. Indeed, a shift to lower value was conjointly observed in the case of **Ar$_1$** and **Ar$_2$** (both from 1643 to 1604 cm^{-1}) and for **Ar$_3$** (from 1646 to 1592 cm^{-1}), while no significant variation occurs for **Ar$_4$** (from 1604 to 1605 cm^{-1}). This shift substantiates a strong interaction of C=N with oxygenated groups (carboxylic acid, alcohol, carbonyl, epoxide) located on the edges of the exfoliated sheets of graphene oxide. Similar downshift was already reported using montmorillonite as filler during aldehyde condensation on chitosan films.(Chabbi et al., 2018) This variation was attributed to the hydrophilic outer surface of C=N that interacts with the surrounding Si—OH and Si—O—Si groups of the mineral clay (Chabbi et al., 2018). To sum up, beside the covalent anchorage of the aromatics within chitosan backbone through C=N linkage and the exfoliation of graphene oxide inside of the network, strong hydrogen-bonding occurs simultaneously between the three partners: chitosan, oxygenated groups of the aromatics and those of graphene oxide sheets (See below).

UV-visible spectroscopy further consolidates the presence of conjugated aromatics inside of the casted films (**Fig. S2** in Sup info). Owing to the presence of glucosamine and N-acetylglucosamine, chitosan **CS-*f*** film displays a typical band with λ_{max} around 200 nm. UV–vis spectra of **CS-Ar$_x$-*f*** nanocomposites show additional absorption bands at 190–240 nm assignable to n-π* and π-π* transition of aryl groups. Indeed, **CS-Ar$_1$-*f***, **CS-Ar$_2$-*f***, **CS-Ar$_3$-*f*** and **CS-Ar$_4$-*f*** display respectively λ_{max} at 210, 205, 203, and 230 nm. In the ternary **CS-Ar$_x$-GO-*f***, λ_{max} was observed at 203, 230, 205, and 210 nm for **CS-Ar$_1$-GO-*f***, **CS-Ar$_2$GO-*f***, **CS-Ar$_3$-GO-*f*** and **CS-Ar$_4$-GO-*f***, respectively.

X-ray diffraction of native **CS-*f*** displays typical peaks at 2θ = 3.66° (2.40 nm) and 5.51° (1.60 nm) attributed to anhydrous crystals and a broad peak around 2θ = 20° (0.44 nm) very characteristic of the amorphous polysaccharide skeletal (Yang et al., 2010). **CS-Ar$_x$-*f*** shows almost similar profile as **CS-*f*** films, with the presence of minor peaks assignable to aromatics, indicating their great dispersion within the carbohydrate network, probably as interdigitated layers H-bonded between chitosan chains (**Fig.**

Published in : Carbohydrate Polymers (2020), vol. 230, 115634
DOI: 10.1016/j.carbpol.2019.115634
Status : Postprint (Author's version)

S3, ESI). A completely different profile was observed by introduction of graphene oxide where we noticed a significant decrease of the amorphous peak of chitosan in **CS-GO-*f*** and in **CS-Ar$_x$-GO-*f*** (Ordikhani, Ramezani Farani, Dehghani, Tamjid, & Simchi, 2015). The disappearance of layered peak of graphene oxide, commonly observed at 2θ of 9.7° (d =0.92 nm) suggests a complete exfoliation of the graphene oxide sheets by chitosan. This delamination is facilitated by two factors: i) first, the use of lower amount of the filler (3 wt% with respect to the biopolymer) and ii) second, the presence in chitosan of nitrogen-containing amine and acetamide groups that are prone to interact with oxygenated groups (epoxides, alcohols and carboxylic acids) of graphene oxide (Frindy et al., 2017; Katir et al., 2019). In the special case of **CS-Ar$_2$-GO-*f*** and **CS-Ar$_4$-GO-*f***, the signature of **Ar$_2$** and **Ar$_4$** are observed indicating their packing inside of the films, with even bulk crystallization observed for **Ar$_4$**. In **CS-Ar$_1$-GO-*f*** and **CS-Ar$_3$-GO-*f***, the conjugated aromatics are well dispersed in the matrix. This indicates that different scenarios of hydrogen bonding occur depending on the position of the substituents with respect to aldehyde in the aryl ring.

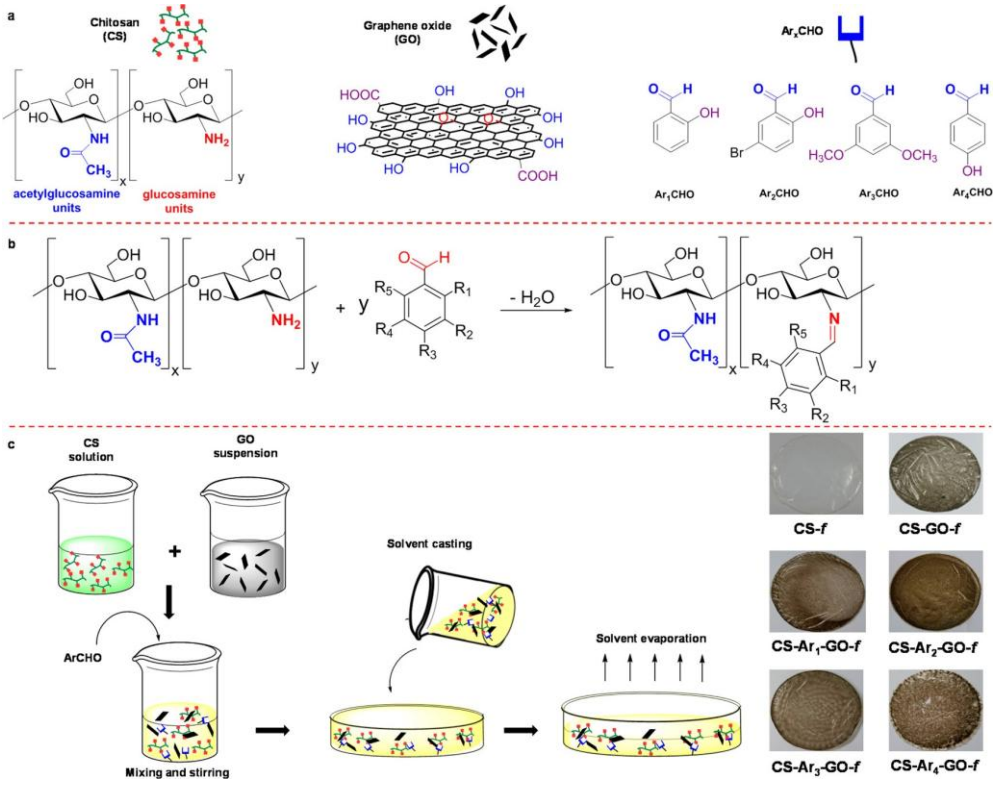

Fig. 1. Schematic illustration of the preparation of aldehyde-functionalized chitosan-graphene oxide glucodynamers. a. the three building-blocks used for nanocomposite design (chitosan; graphene oxide, aldehydes). b. Schiff-base condensation of chitosan-to-aldehyde. c. step-by-step preparation of modified chitosan films and digital photos of the functionalized nanocomposite films.

The microstructure of **CS-*f***, **CS-Ar$_x$-*f***, **CS-GO-*f*** and **CS-Ar$_x$-GO-*f*** was investigated by scanning and transmission electron microscopies (SEM and TEM). Owing to its high transparency, non-modified chitosan film **CS-*f*** can be easily distinguished from those built from **CS-Ar$_x$-*f***, **CS-GO-*f*** and **CS-Ar$_x$GO-*f***. SEM revealed indeed that native chitosan film displays a typical uniform morphology and very smooth surface without defects or porosity (**Figs. 3** and **S4** in Sup info). In contrast, parallel lines induced by crystallization were observed in the case of **CS-Ar$_4$-*f*** and the presence of voids and porous network was

Published in : Carbohydrate Polymers (2020), vol. 230, 115634
DOI: 10.1016/j.carbpol.2019.115634
Status : Postprint (Author's version)

noticed in the case of **CSAr$_3$-*f***. In **CS-GO-*f***, homogenous distribution was observed and no isolated sheets or aggregates can be observed, in line with the exfoliation of individual sheets alone the biopolymer. However, in the ternary **CS-Ar$_x$-GO-*f***, a slight surface roughening was observed and a porous network was also generated in the case of **CS-Ar$_3$-GO-*f***. The porosity observed in **CS-Ar$_3$-*f*** and **CS-Ar$_3$-GO-*f*** can be attributed to the phase separation induced by this bulky aromatic that grows probably out of water during aldehyde-to-amine condensation (Marin et al., 2014). The similarity in the surface-state between **CS-Ar$_x$-*f*** and **CS-Ar$_x$-GO-*f*** evidenced the pivotal role of aromatic rings in altering the secondary structure of the biopolymer through hydrogen-bonding and π-π stacking interactions. Similar results were also reported during chitosan functionalization by salicylaldehyde and 4-benzaldehyde in the presence of montmorillonite clay sheets (Chabbi et al., 2018). EDX mapping was used to confirm the existence of expected chemical elements and the purity of the films (**Fig. S5** in Sup info). Only peaks corresponding to carbon, oxygen and nitrogen elements (respectively at 2.26, 0.52 and 0.38 Kev) were observed for films functionalized with **Ar$_1$**, **Ar$_3$** and **Ar$_4$**. In **CS-Ar$_2$-*f***, an intense peak was also observed at 1.49 keV assignable to bromide fragment, in superb agreement with the chemical structure of **Ar$_2$**. TEM analyses reveal the presence of dark lines and expanded spots attributed to graphene oxide sheets that are entangled in the network of **CS-Ar$_x$-GO-*f*** and probably connected through π-π stacking and hydrogen bonding to aryl groups. Distinctively, no similar lamellar structure could be detected within **CS-Ar$_x$-*f*** (**Fig. 3**).

Wettability of chitosan films was also measured depending on the presence of aromatics or both aromatics and graphene oxide filler (**Fig. 3** and **Table S1** in Sup info). Native chitosan film displays a contact angle value of ~ 112.6° (± 1.66). Whatever the conjugated aromatic, a decrease of the wettability was noticed for **CS-Ar$_x$-*f*** compared to **CS-*f***. These values range from 85° (±1.38) **for CS-Ar$_4$-*f*** to 100.2° (±1.99) for **CS-Ar$_1$-*f***. A significant decrease to 100.9° (± 2.20) was also experienced for **CS-GO-*f***. Further decrease was even noticed for the ternary **CS-Ar$_x$-GO-*f*** where the wettability ranges from 87.1° (±2.22) for **CS-Ar$_1$-GO-*f*** to 66.1° (±3.07) for **CS-Ar$_4$-GO-*f***. While one may expect an increase in the contact angle because of the hydrophobic character of the graphene oxide layers, the opposite trend was observed herein. This can be tentatively explained by several factors: i) the presence of numerous oxygen groups belonging either to graphene oxide and aromatics as well as the formation of polar C=N, easily exposed to the water-droplet compared to NH_2 groups, more buried in the entangled network. ii) Wettability can be also affected by the surface-state of the shaped films. Considering that **CS-Ar$_x$-*f*** and **CS-Ar$_x$-GO-*f*** display rough surface with the presence of pores and stacked crystals, this discrepancy might be the origin of increasing surface wettability. Notably, even the position of the substituent is pivotal in determining the surface energy of the conceived films, as illustrated by the difference in the contact angle measurement of *ortho*- and *para*-hydroxybenzaldehyde **Ar$_1$** and **Ar$_4$**. The following figure illustrates the plausible interplay occurring between chitosan, the aromatics and graphene oxide sheets (**Fig. 4**).

Published in : Carbohydrate Polymers (2020), vol.230, pp. 115634
DOI: 10.1016/j.carbpol.2019.115634
Status : Postprint (Author's version)

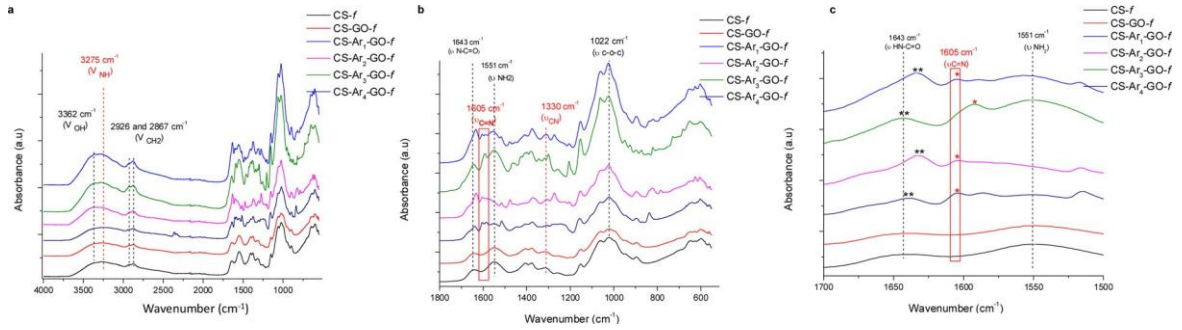

Fig. 2. Typical DRIFT spectra of **CS-Ar$_x$-GO-*f*** (a) the full spectra, (b) high magnification (1800–600cm^{-1}) and (c) the stars showing chemical shift for the newly created (C]N) imine bonds.

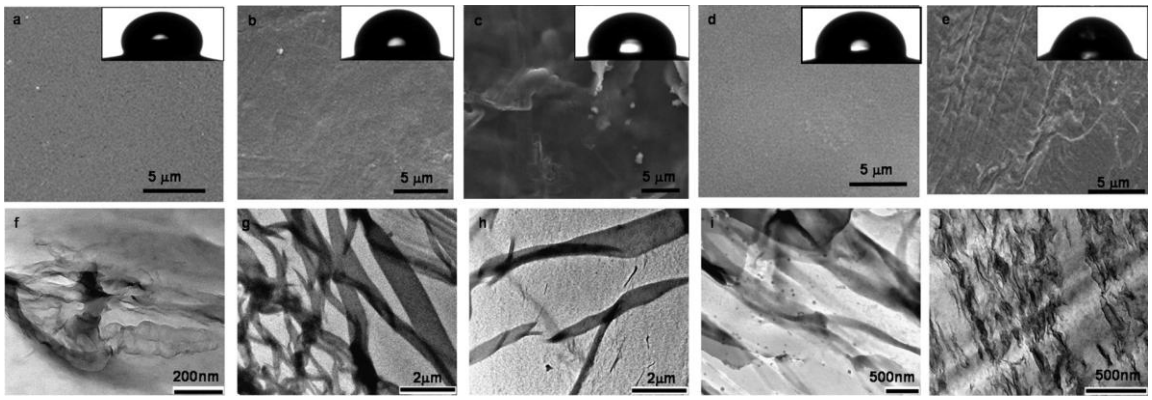

Fig. 3. A-e Scanning electronic microscopy analyses and contact angle measurement (onset) of : a) **CS-GO-*f***; b) **CS-AR$_2$-GO-*f***; c) **CS-Ar$_2$-GO-*f***; d) **CS-Ar$_3$-GO-*f***; e) **CS-Ar$_4$-GO-*f***. f-j Transmission electronic microscopy analyses of. f) **CS-GO-*f***; g) **CS-Ar$_1$-GO-*f***; h) **CS-Ar$_2$-GO-*f***; i) **CS-Ar$_3$-GO-*f***; j) **CS-Ar$_4$-GO-*f***.

3.2. THERMAL BEHAVIOR AND MECHANICAL PROPERTIES OF ALDEHYDEFUNCTIONALIZED FILMS

Functional chitosan films were next subjected to thermal gravimetric analysis and differential scanning calorimetry measurements (**Fig. 5**). Thermal degradation of chitosan involves three different stages, starting with the first step between room temperature and 100 °C, attributed to the evaporation of water weakly bonded or physically entrapped in chitosan network. The second degradation step occurring between 150 °C and 210 °C corresponds to an extended dehydration, deacetylation and early depolymerization of glycoside units of chitosan. Finally, the third weight loss takes place above 300 °C to convert small oligomeric chitosan to carbon or even mineralize them into volatiles (Hong et al., 2007). An improvement of the material stability was reached by chemical grafting of aromatics into chitosan in **CS-Ar$_x$-*f*** and in **CS-Ar$_x$-GO-*f***. The faster degradation of chitosan occurring between 100 °C and 200 °C was significantly delayed in **CS-Ar$_x$-*f*** and **CS-Ar$_x$-GO-*f*** but not in the case of **CS-GO-*f*** (Frindy et al., 2017). This indicates that the conjugation of aromatic within the carbohydrate backbone drives water outside of the films and reduces significantly the moisture uptake, making them more hydrophobic. Hence, the main reason for decreasing the contact angle measurement can be attributed to the roughness of the surface and not to the change in the hydrophilic-hydrophobic balance of the composite. **CS-GO-*f*** alone does not exhibit similar behavior because of the degradation of oxygenated groups of graphene oxide occurring between 100 °C and 200 °C (Jia, Gai, Wang, & Zhao, 2016; Ordikhani et al., 2015; Yadav & Ahmad, 2015). Within the **CS-Ar$_x$-*f*** materials, functionalization with **Ar$_1$**

Published in : Carbohydrate Polymers (2020), vol.230, pp. 115634
DOI: 10.1016/j.carbpol.2019.115634
Status : Postprint (Author's version)

(salicylaldehyde) provides more stable films compared to *meta*- and *para*-hydroxy-benzaldehyde. The delayed degradation observed for **CS-Ar$_1$-*f*** film can be attributed to the great dispersion of both **Ar$_1$** and **GO** in chitosan that form, after evaporation, dense and packed network; the latter do not allow faster propagation of the heat inside. Differential scanning calorimetry (DSC) was further investigated over a temperature range between room temperature and 250 °C, with a single heating cycle (**Figs. 5**, **S6** in Sup info and **Table S1** in Sup info). All films showed a single net and wide endothermic peak centered around 100 °C, except **CS-Ar$_4$-*f*** that displays an acute peak at 114 °C. Another weakly intense exothermic peak was observed between 200 °C and 250 °C, indicating the decomposition of chitosan films (Cervera et al., 2004; Nunthanid, Puttipipatkhachorn, Yamamoto, & Peck, 2001). Peaks around 100 °C are attributed to the loss of water, where we noticed a significant increase in the temperature in the case of **Ar$_1$** and **Ar$_4$**. Enthalpy values associated to this adsorption increased in all **CS-Ar$_x$-*f*** with respect to **CS-*f*** alone (Cervera et al., 2004). Similar increase in water removal temperature was observed for **CS-Ar$_x$-GO-*f*** with respect to **CS-GO-*f*** with even, a significant increase of the dehydration enthalpy value being associated to the conjugation of aromatics. This appears in agreement with the increase in the percentage of the water amount at temperature around 100 °C (dos Santos, Dockal, & Cavalheiro, 2005; Mahmoudi, Ostadhossein, & Simchi, 2016; Tirkistani, 1998).

Mechanical properties of **CS-Ar$_x$-GO-*f*** were next investigated and compared to those of **CS-*f***, **CS-GO-*f*** and **CS-Ar$_x$-*f***. Tensile strength and elongation at break of the films are presented as the typical stress-strain curves (**Fig. S7** in Sup info). The in situ addition of 3 wt% graphene oxide into the chitosan solution improves the tensile properties of the resulting films, by an increase from 30 MPa in **CS-*f*** to 44 MPa for **CS-GO-*f***, similarly to what has been reported in other studies (Song, Wang, & Chang, 2014; Yang et al., 2010). On the other hand, a greater lengthening of the **CS-GO-*f*** film can be observed compared to the native **CS-*f***. This increase in resistance can be related to the dispersion of **GO** sheets and the strong interfacial interactions between chitosan and graphene oxide. A remarkable increase of the Young Modulus was noticed for **CS-GO-*f*** compared to native **CS-*f*** chitosan film (**table S1** in Sup info) (Dinu, Cocarta, & Dragan, 2016; Han et al., 2011; Mohammadi, Mesgar, & Rasouli-Disfani, 2016; Yadav et al., 2013; Yuan et al., 2014). When the conjugated aromatics are well-dispersed, their incorporation resulted also in an increase in the mechanical properties. Indeed, the stacked **Ar$_4$** within **CS-Ar$_4$-*f*** displays poor flexibility among the newly prepared films. In turn, high tensile strength and flexibility are reached for **CS-Ar$_1$-*f***, which has been identified as the most successfully dispersed aromatic within the film series. Spectacular improvement was also observed for **CS-Ar$_2$-GO-*f*** and **CS-Ar$_3$-GO-*f*** owing to the simultaneous presence of graphene oxide filler and interdigitated aromatics (**Fig. 6**). The presence of the aromatic units between the chains of chitosan is suspected to increases the polymer-polymer and polymer-**GO** interaction (probably through π-π stacking). This resulted in increasing both the tensile strength and the flexibility of the films. Notably, because of some irregularities seen in the film and the difficulties in having a homogenous thickness, precautions are still needed in interpreting the observed trend. However, one of the most important facts gleaned from this study is the possible integration of the active aromatic ingredients inside of chitosan-graphene oxide without destroying its mechanical properties and that delightfully, self-standing biodynamic films can be prepared through this route.

Published in : Carbohydrate Polymers (2020), vol.230, pp. 115634
DOI: 10.1016/j.carbpol.2019.115634
Status : Postprint (Author's version)

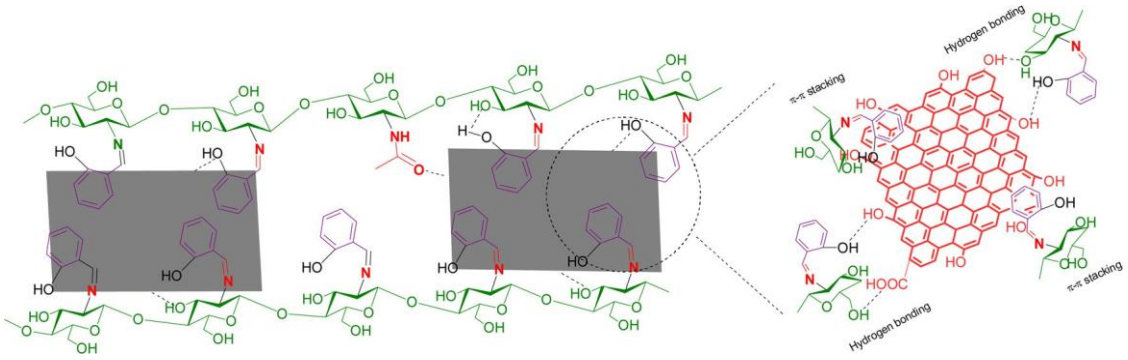

Fig. 4. A plausible structure of the ternary nanocomposites showing the interplay of the three players: chitosan, graphene oxide and the aromatics.

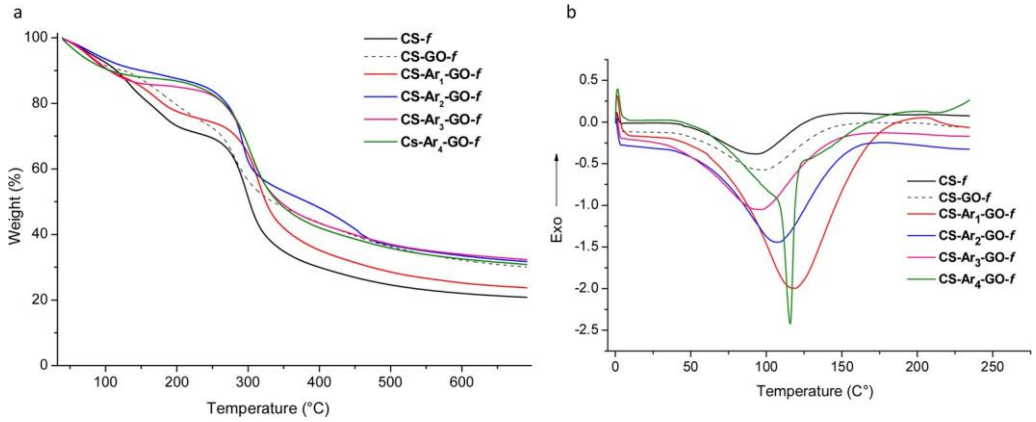

Fig. 5. A plausible structure of the ternary nanocomposites showing the interplay of the three players: chitosan, graphene oxide and the aromatics.

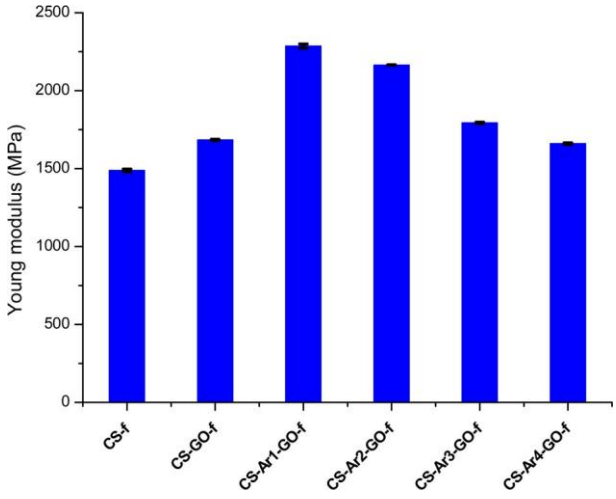

Fig. 6. Young's modulus of **CS-*f***, **CS-GO-*f*** and **CS-Ar$_x$-GO-*f***.

Published in : Carbohydrate Polymers (2020), vol.230, pp. 115634
DOI: 10.1016/j.carbpol.2019.115634
Status : Postprint (Author's version)

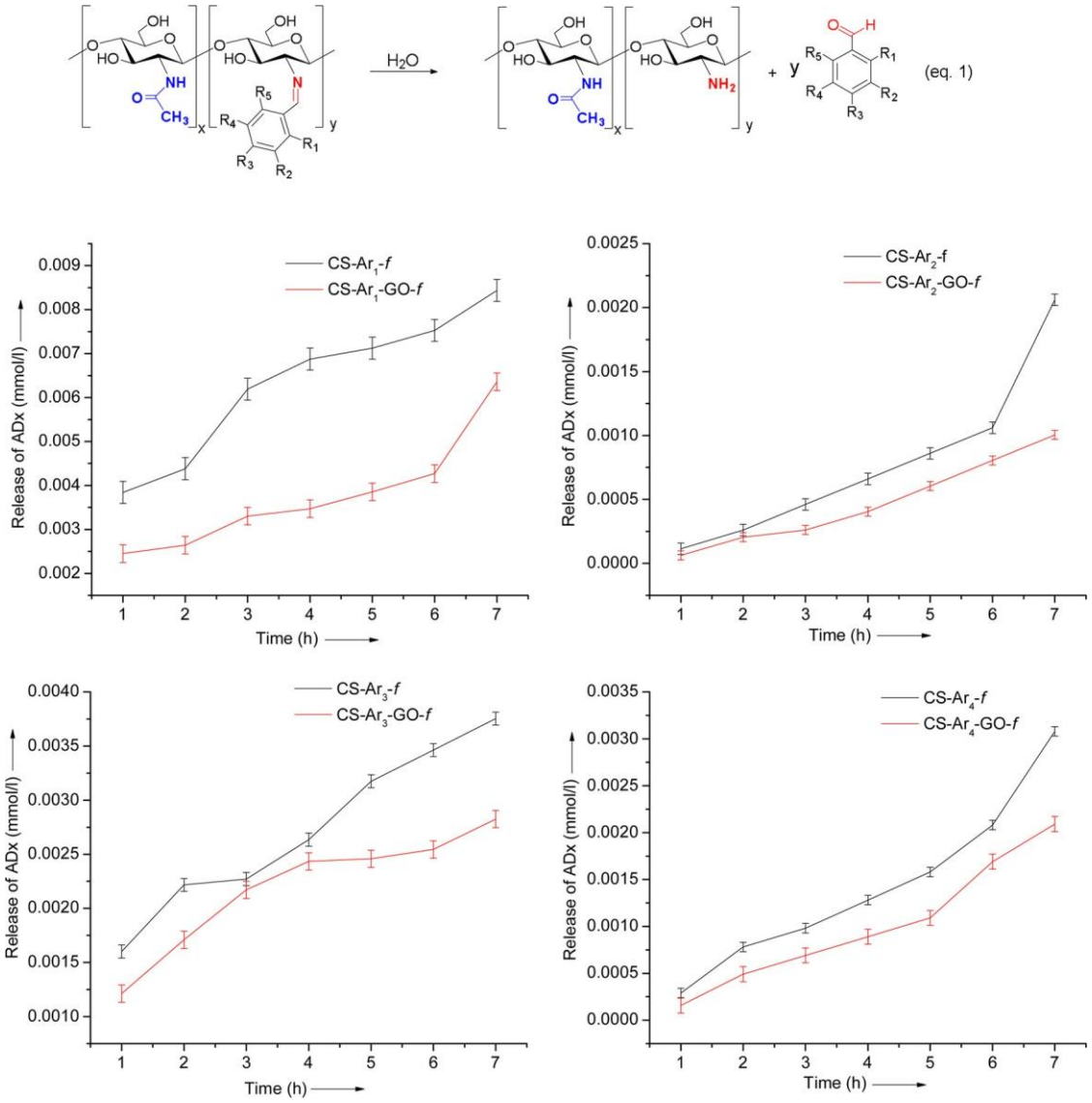

Fig. 7. Comparison of the kinetic release of Ar_x from the bioplastic depending on the presence or not of the graphene oxide.

3.3. RELEASE OF ALDEHYDES IN FUNCTIONALIZED CHITOSAN FILMS

We have selected chitosan conjugation to aldehyde because it afford C=N bonding linkage. The so-called imine stands as efficient toolbox in dynamic chemistry because of its reversible nature (Antony et al., 2019; Godoy-Alcántar et al., 2005; Schiff, 1864). Beyond chemical uptake and release, imine-featuring systems have already demonstrated their efficiency in machinery, self-healable and programmable materials (Dohno et al., 2005). Notably, few dynamic systems shaped as films are known and no one based on sustainable bioplastic was reported so far. In our case, chitosan plays two roles: it constitute the matrix because of its film-forming ability and it serve also to conjugate the aromatics through its amino groups. Because of the sensitivity of C=N bonds to water, immersing the film in aqueous medium will release the aromatic to the solution (eq.1). In such a way, the as-prepared films can be used to catch and release chemicals for various applications (*ex*. in agricultural for

Published in : Carbohydrate Polymers (2020), vol.230, pp. 115634
DOI: 10.1016/j.carbpol.2019.115634
Status : Postprint (Author's version)

delivering fertilizers to the soil). In these biodynamer systems, the release should be triggered by extra stimulus in a time-controlled manner. The progressive release is mandatory for avoiding undesirable effects associated to supersaturation and accumulation of the chemicals in the medium. We consequently embarked to study chemical release in **CS-Ar$_x$-GO-*f*** depending on the pH variation, temperature increase and as a function of time.

At a first glance, the chemical release from these films was found to be dependent on the starting aromatics and the presence or not of graphene oxide (**Fig.7**). Generally, whatever the aromatic used, the release is delayed in **CS-Ar$_x$-GO-*f*** compared to **CS-Ar$_x$-*f***. The occurrence of this phenomenon irrespective to the position of oxygenated substituents suggests that the aromatics strongly interact with graphene oxide through π-π stacking of the benzene ring rather than via oxygenated functional groups. This behavior contrasts the one observed with polar MMT where the edges features several Si—OH groups and even the basal Si—O—Si allow for interacting with the aromatics depending on their substituents position. Within the aromatic series, **Ar$_1$** records the highest release both in **CS-Ar$_1$-*f*** and **CS-Ar$_1$-GO-*f*** while the lowest release was recorded for **Ar$_4$** in both **CS-Ar$_4$-*f*** and **CS-Ar$_4$-GO-*f***, probably because of its tendency to aggregate and the formation of bulky crystals. Faster release can be thermally-induced because rising temperature accelerates C=N hydrolysis in **CS-Ar$_x$-*f*** and **CS-Ar$_x$-GO-*f*** films (**Fig. S8**, ESI in Sup info). Variation in pH reveals also an enhanced imine hydrolysis under acidic and basic conditions for **CS-Ar$_x$-*f***, in agreement with the sensitivity of C=N under acid and basic medium (**Fig. S10**, ESI in Sup info). In **CS-Ar$_x$-GO-*f***, while hydrolysis occurs under acidic medium, only moderate increase was observed under basic conditions, which might point to the involvement of graphene oxide surface to scavenge Na^+ and/or OH^- from the medium (**Fig. S9**, in Sup info). It is known that graphene oxide is slightly acidic and this property is at the basis of its use as heterogeneous acid catalyst (Garg, Bisht, & Ling, 2014). Beside hydroxyl and carboxylic acid groups that are prone to react with Na^+, the surface of graphene oxide features also highly acidic sulfonate derivatives that emanate from Hummer treatment and are reliable to interact with sodium cations (Wu, Liang, Ma, Lu, & Xiang, 2019). In any case, these unprecedented results evidence the dual role of the filler not only for improving the mechanical properties of the films but also for influencing the release kinetic of the conjugated chemicals. Future work will be devoted to the use of more biologically relevant aldehydes (both commercially-available, biomass-based or synthetic ones), their sequestration inside of the bioplastics and their synergistic action for improving the antioxidant and antibacterial activity and oxygen permeability (Crouvisier-Urion et al., 2019). It will be also interesting to covalently bond two different biologically-active aldehydes and to assess their sequential release in water medium (Hsu et al., 2014).

4. Conclusions

Novel ternary functionalized glucodynamic films, denoted as **CS-Ar$_x$-GO-*f***, are designed by reacting *ortho*-, *meta*- and *para*- substituted aromatic aldehyde on colloidal chitosan –graphene oxide solution following an evaporative-induced film-assembly process. The incorporation of graphene oxide confers interesting properties to the reinforced films as illustrated by their surface wettability, hydrophobicity and improved mechanical properties. The presence of organic molecules did not alter the flexibility of these films and the mechanical properties of aldehyde-conjugated chitosan were not affected by its

Published in : Carbohydrate Polymers (2020), vol.230, pp. 115634
DOI: 10.1016/j.carbpol.2019.115634
Status : Postprint (Author's version)

derivatisation, allowing for shaping these materials are crack-free bioplastic films. Notably, chitosan plays two roles: it constitute the matrix because of its film-forming ability and it serve also to conjugate the aromatics through its amino groups. When the film is immersed in water medium, the attachment between chitosan and the aromatics is cleaved (hydrolysis of C=N imine) and the aromatics escape from the film to the aqueous solution. Whatever the aromatic used, a significant delay on aldehyde release was observed in **CS-Ar$_x$-GO-*f*** compared to **CS-Ar$_x$-*f***, a difference attributed to the presence of graphene oxide. The latter act as a barrier to hinder their escape from the matrix, probably by providing more interacting and/or ligating sites, mainly by π-π stacking and hydrogen-bonding. Hitherto, common use of nano-sized fillers is dictated by improvement of thermal and mechanical properties. We herein demonstrate that beyond this conventional wisdom, graphene oxide acts as a regulator for the aldehyde release from functionalized chitosan-based nanocomposites. Moreover, depending on the polarity of the filler, different scenarios are observed, which suggest that merging hydrophilic MMT and hydrophobic graphene oxide in the polysaccharide network can further adjust these properties. Overall, this yet-unexplored field will expand the use of bio-based nanocomposite materials to key domains that involve matter storage and release. Further investigations are necessary to fully understand the biological properties and adverse effects of these materials, both individually (graphene oxide, chitosan) and in combination.

Acknowledgment

JC thanks Erasmus + for his mobility. UEMF, Projet Prioritaire (PPR1/2015/73; MESRSFCCNRST) and Hassan II academy of Science and Technology are acknowledged for their funding.

Published in : Carbohydrate Polymers (2020), vol.230, pp. 115634
DOI: 10.1016/j.carbpol.2019.115634
Status : Postprint (Author's version)

Appendix A. Supplementary data

Table 1: Contact Angle, thermal analysis and mechanical properties of films :

			DSC analysis		Mechanical properties	
Sample	Contact angle value	Char residue (700°C)	T max (°C)	ΔH (J/g)	Young modulus (MPa)	Stress (MPa)
CS-*f*	112.6° ± 1.66	21%	94	21.44	1488.80 ± 3.92	30 ± 2.3
CS-Ar$_1$-*f*	100.2° ± 1.99	33%	114	73.67	1902.90 ± 3.81	74 ± 1.8
CS-Ar$_2$-*f*	98.3° ± 1.41	32%	94	58.67	1857.83 ± 5.46	77 ± 2.5
CS-Ar$_3$-*f*	94.6° ± 3.30	29%	92	30.51	1746.42 ± 6.63	55 ± 1.4
CS-Ar4-*f*	85° ± 1.38	30%	115	47.43	1624.12 ± 5.57	40 ± 2.9
CS-GO-*f*	100.9° ± 2.20	30%	97	27.45	1684.45 ± 4.09	44 ± 3.2
CS-Ar$_1$-GO-*f*	87.1° ± 2.22	24%	119	120.44	2286.57 ± 2.19	78 ± 2.5
CS-Ar$_2$-GO-*f*	85.3° ± 1.85	32%	108	63.82	2164.45 ± 2.03	78 ± 2.2
CS-Ar$_3$-GO-*f*	82.5° ± 1.91	33%	95	51.48	1794.09 ± 2.57	72 ± 1.5
CS-Ar$_4$-GO-*f*	66.1° ± 3.07	31%	117	65.58	1660.18 ± 5.02	43 ± 2.4

Figure S1: DRIFT analysis of films **GO**, **CS-*f***, **CS-GO-*f*** and **CS-AR$_x$-*f*** :

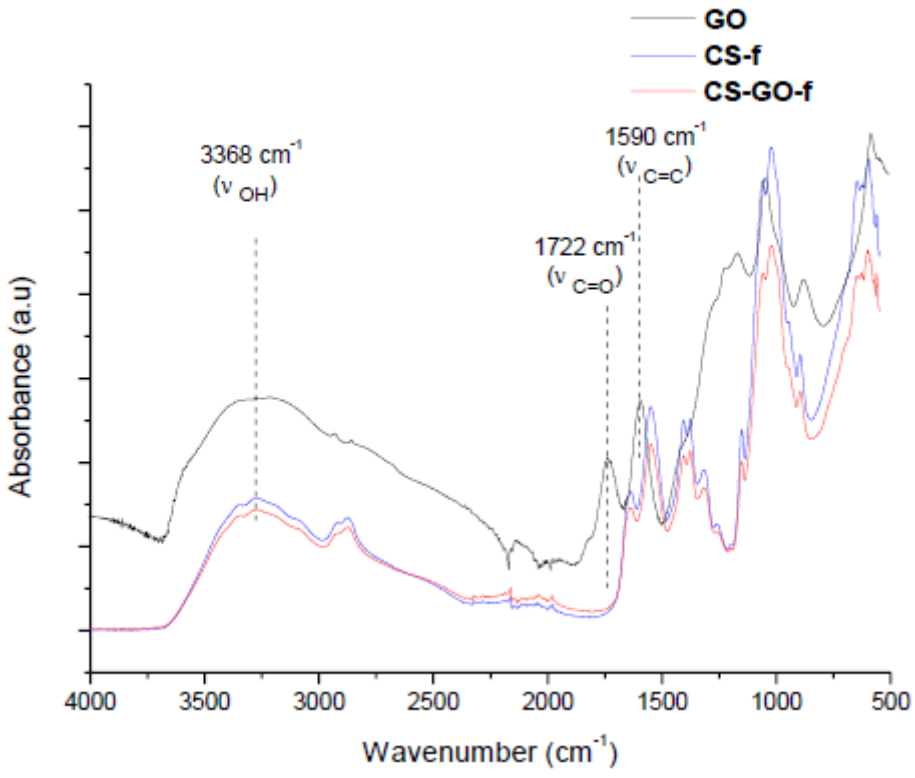

Published in : Carbohydrate Polymers (2020), vol.230, pp. 115634
DOI: 10.1016/j.carbpol.2019.115634
Status : Postprint (Author's version)

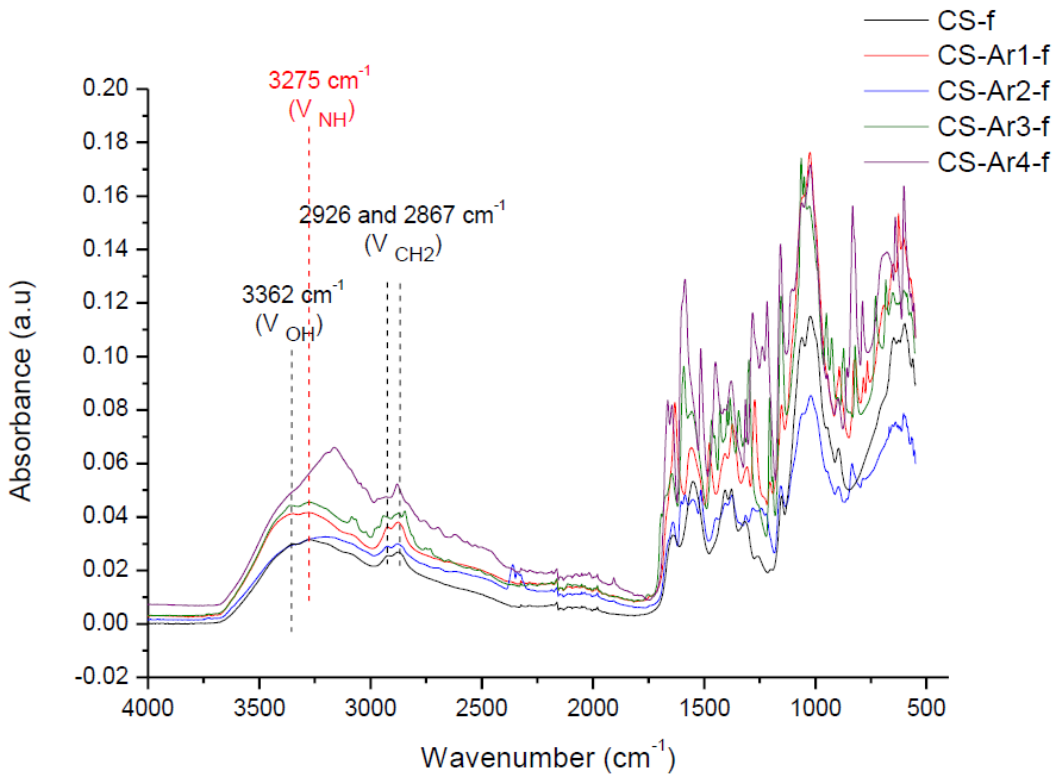

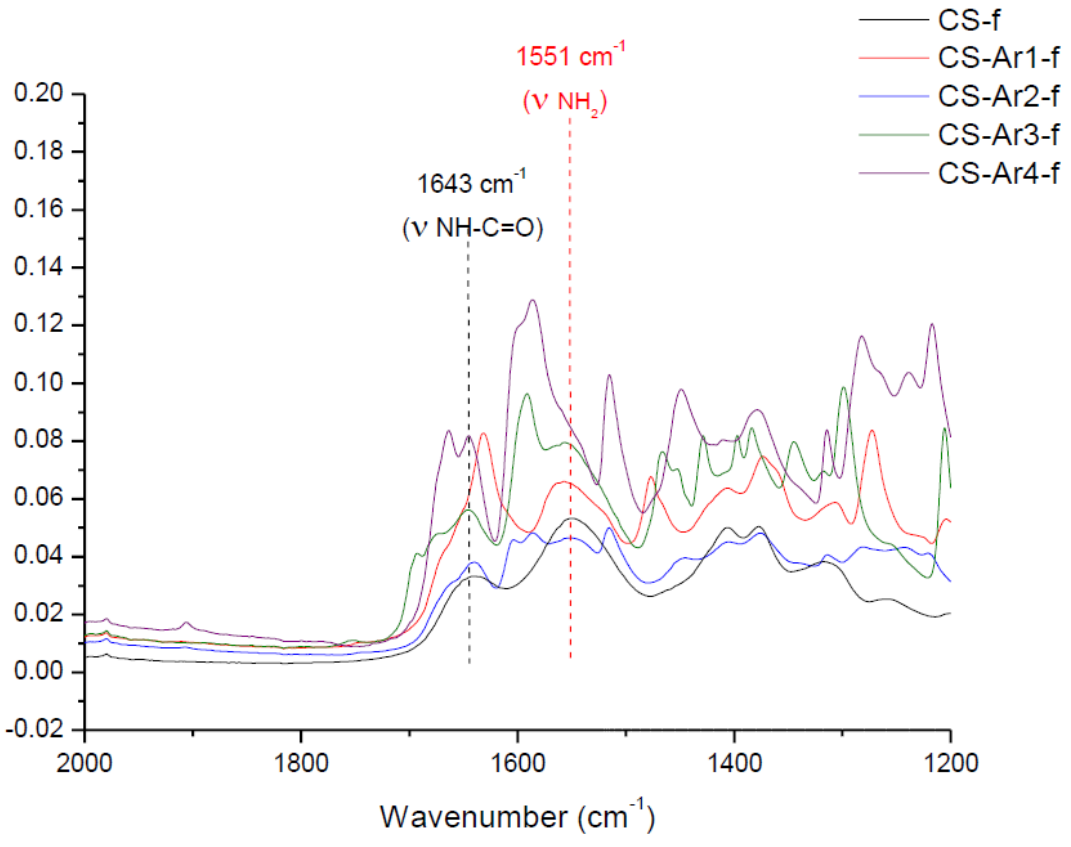

Published in : Carbohydrate Polymers (2020), vol.230, pp. 115634
DOI: 10.1016/j.carbpol.2019.115634
Status : Postprint (Author's version)

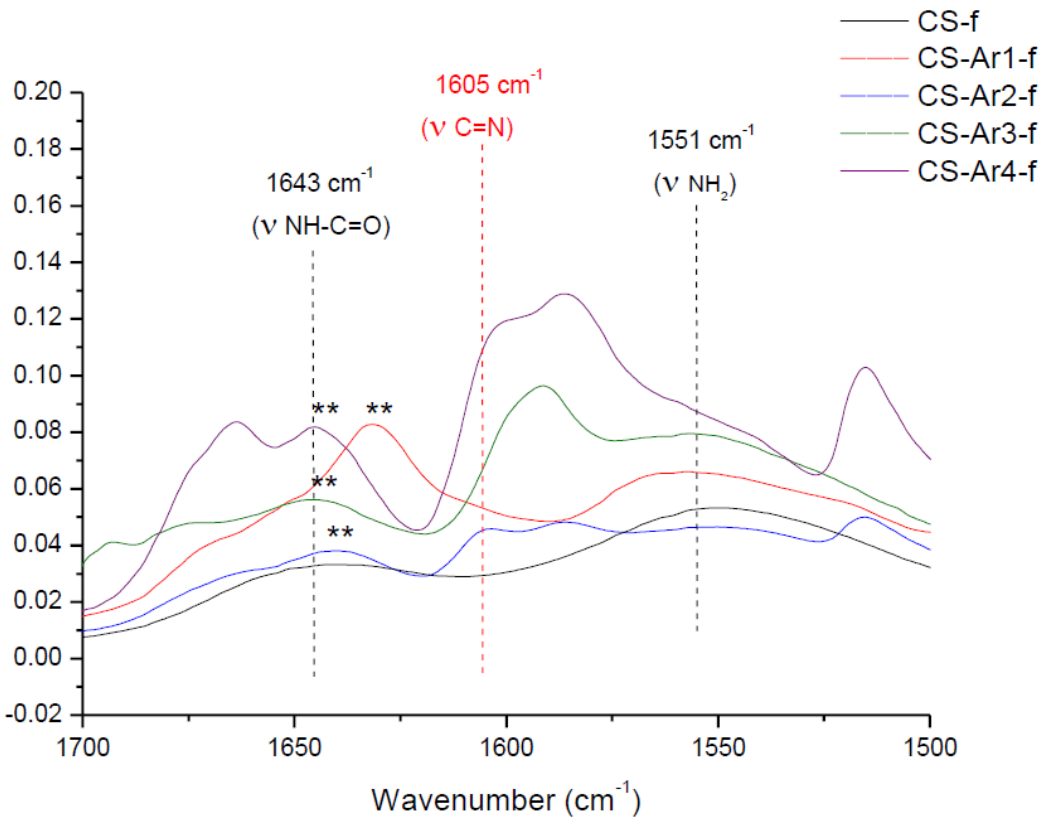

Figure S2: DRUV-visible analysis of films **CS-Ar$_x$-*f*** and **CS-AR$_x$-GO-*f*** :

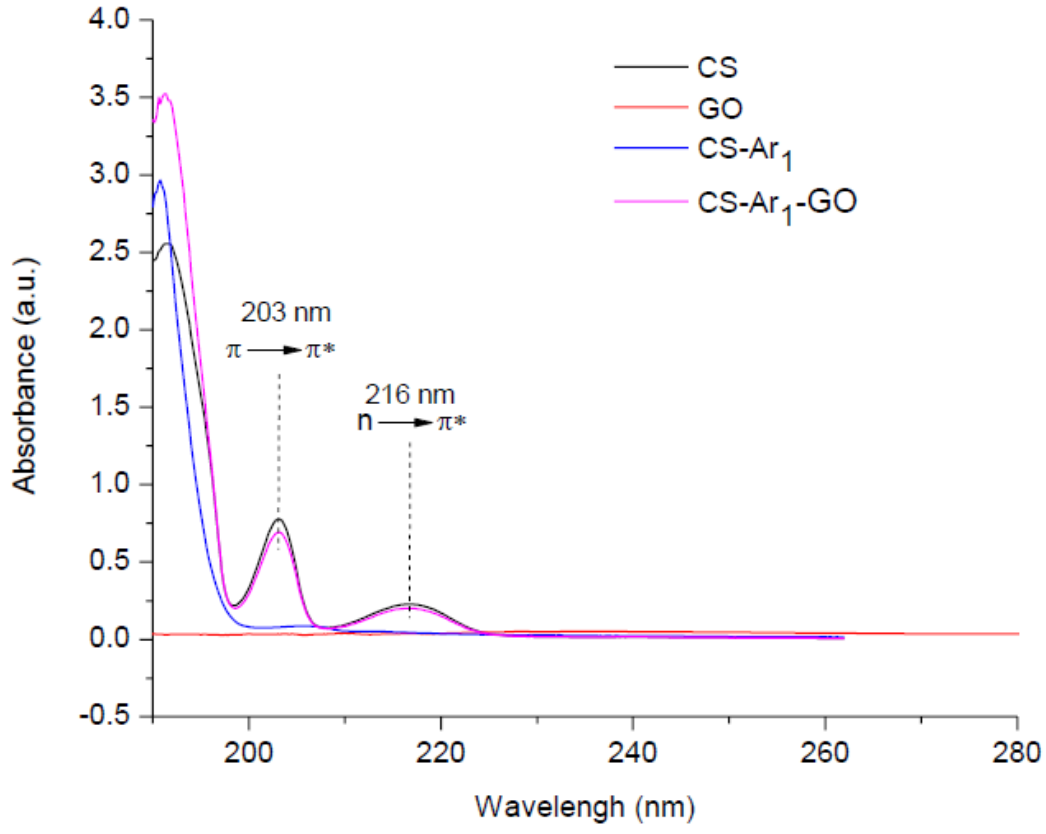

Published in : Carbohydrate Polymers (2020), vol.230, pp. 115634
DOI: 10.1016/j.carbpol.2019.115634
Status : Postprint (Author's version)

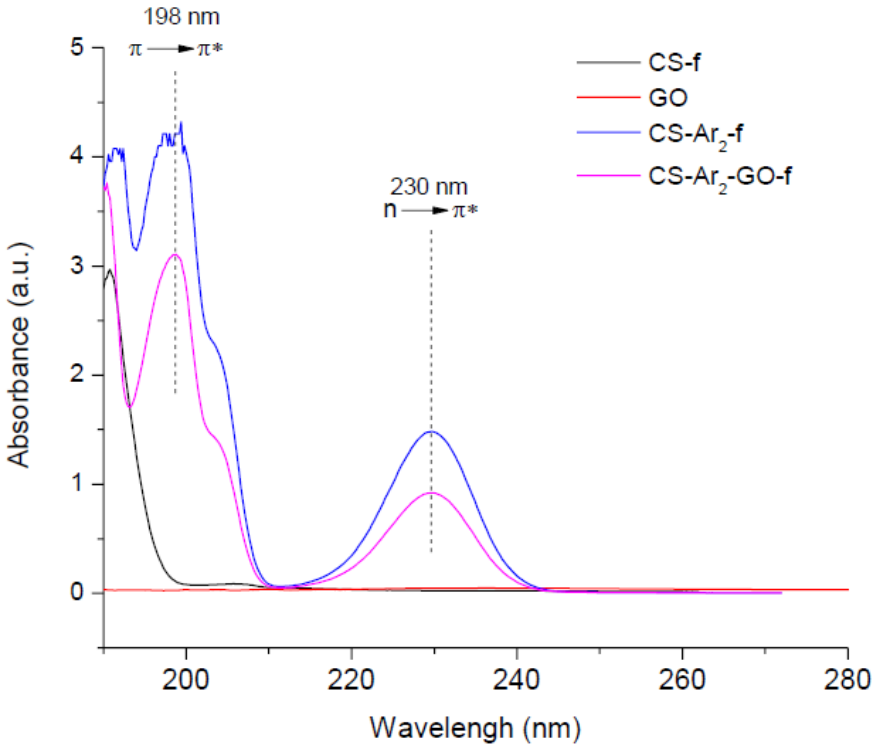

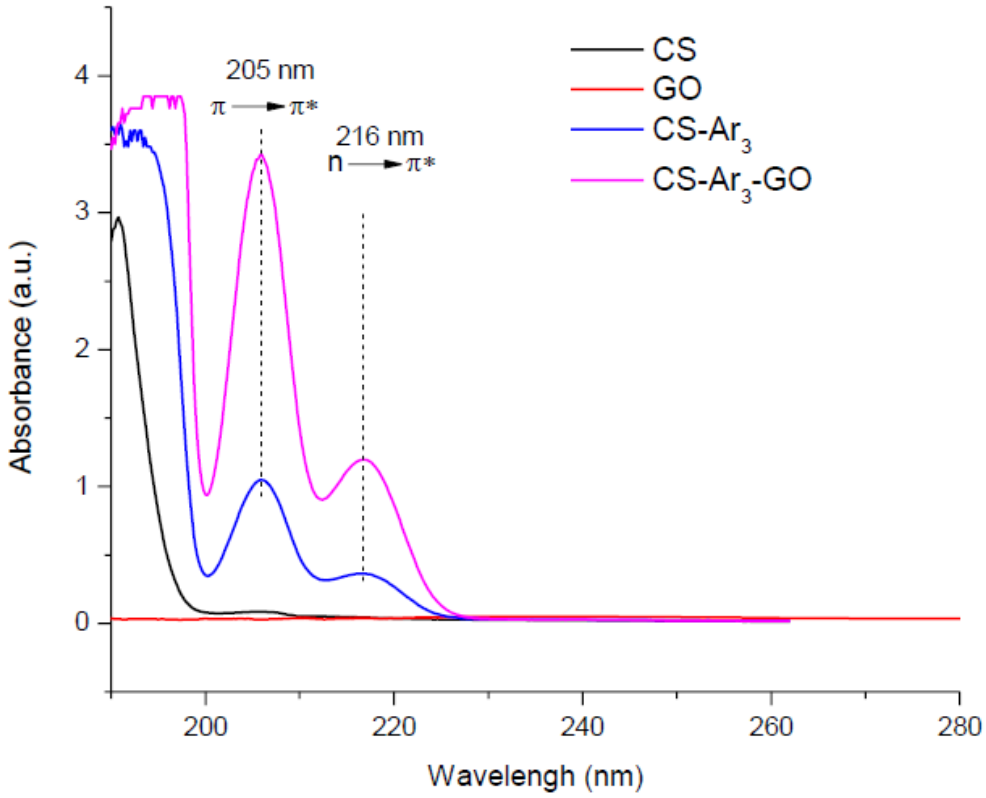

Published in : Carbohydrate Polymers (2020), vol.230, pp. 115634
DOI: 10.1016/j.carbpol.2019.115634
Status : Postprint (Author's version)

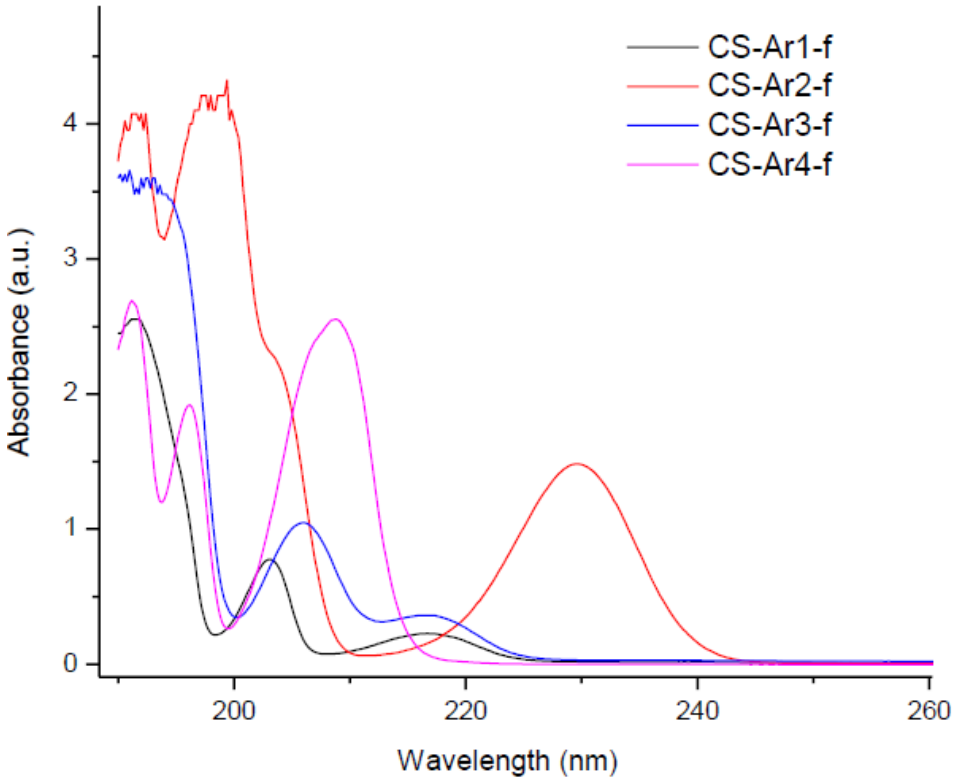

Figure S3: XRD analysis of films :

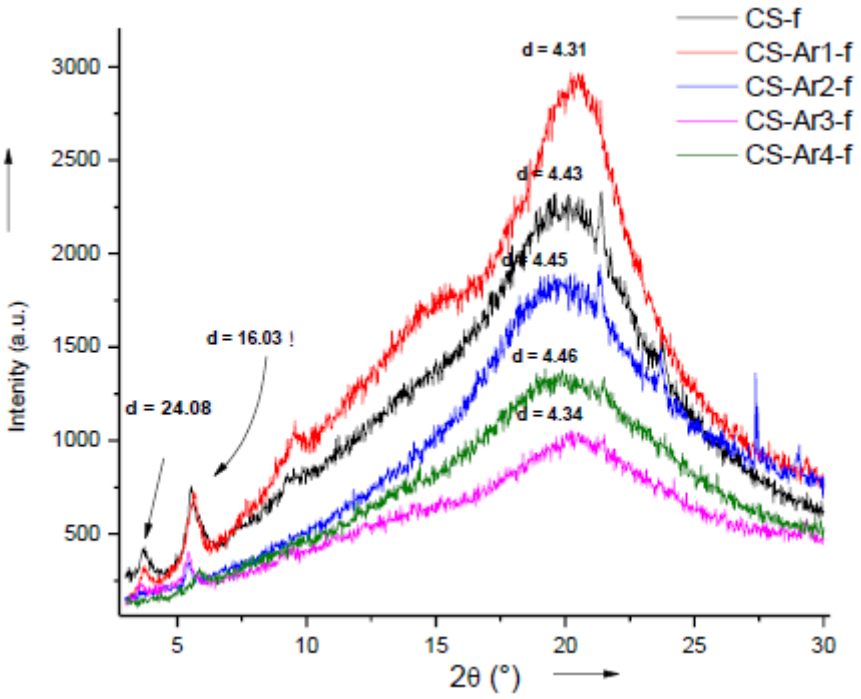

Published in : Carbohydrate Polymers (2020), vol.230, pp. 115634
DOI: 10.1016/j.carbpol.2019.115634
Status : Postprint (Author's version)

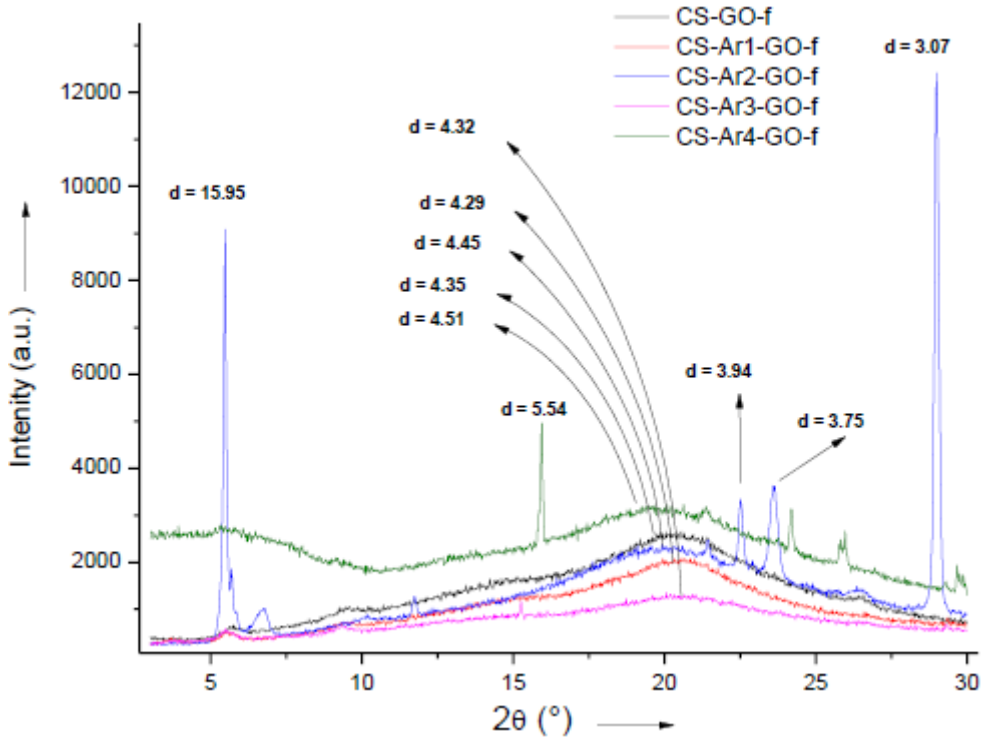

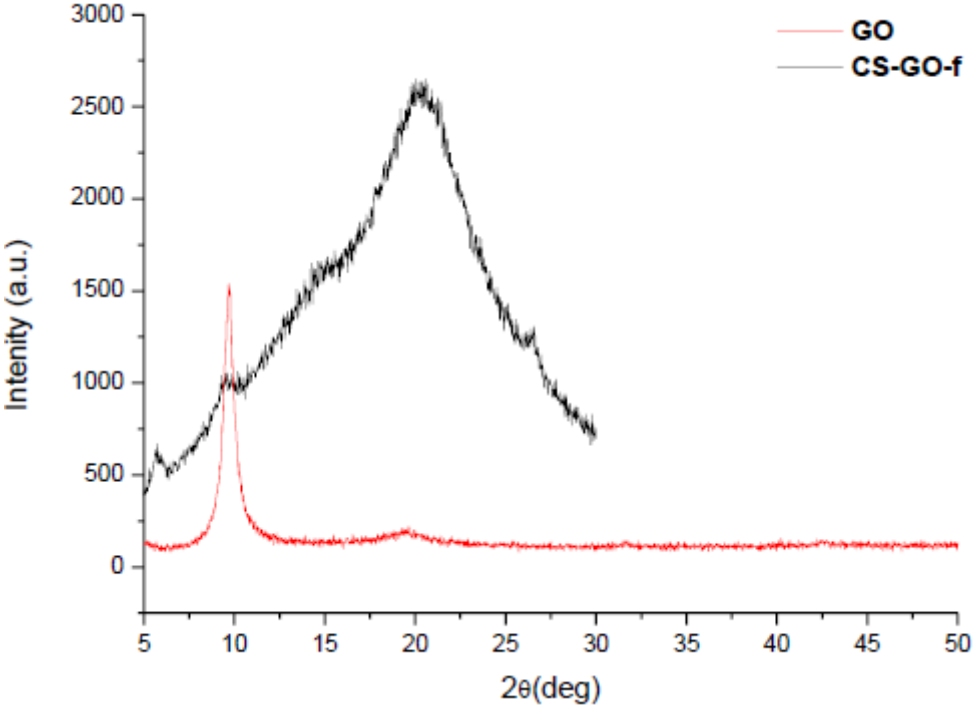

Published in : Carbohydrate Polymers (2020), vol.230, pp. 115634
DOI: 10.1016/j.carbpol.2019.115634
Status : Postprint (Author's version)

Figure S4: Scanning electronic microscopy analyses, contact angle measurement and Transmission electronic microscopy analyses of **CS-Ar$_x$-*f*** :

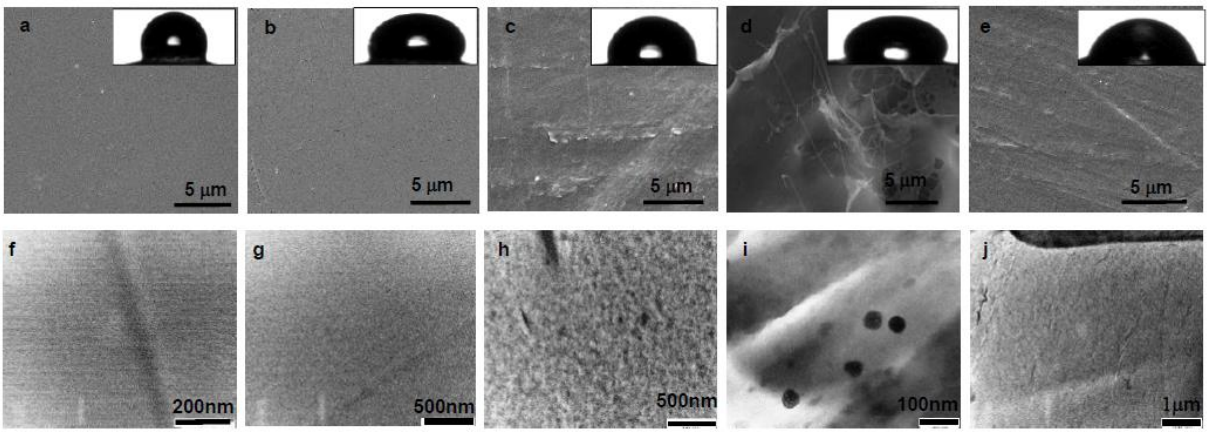

a-e Scanning electronic microscopy analyses and contact angle measurement (onset) of : a) **CS-*f*** ; b) **CS-Ar$_1$-*f*** ; c) **CS-Ar$_2$-*f*;** d) **CS-Ar$_3$-*f*;** e) **CS-Ar$_4$-*f*. f-j** Transmission electronic microscopy analyses of. f) **CS-*f*;** g) **CS-Ar$_1$-*f*;** h) **CS-Ar$_2$-*f*;** i) **CS-Ar$_3$-*f*;** j) **CS-Ar$_4$-*f*.**

Figure S5: EDX analysis of films :

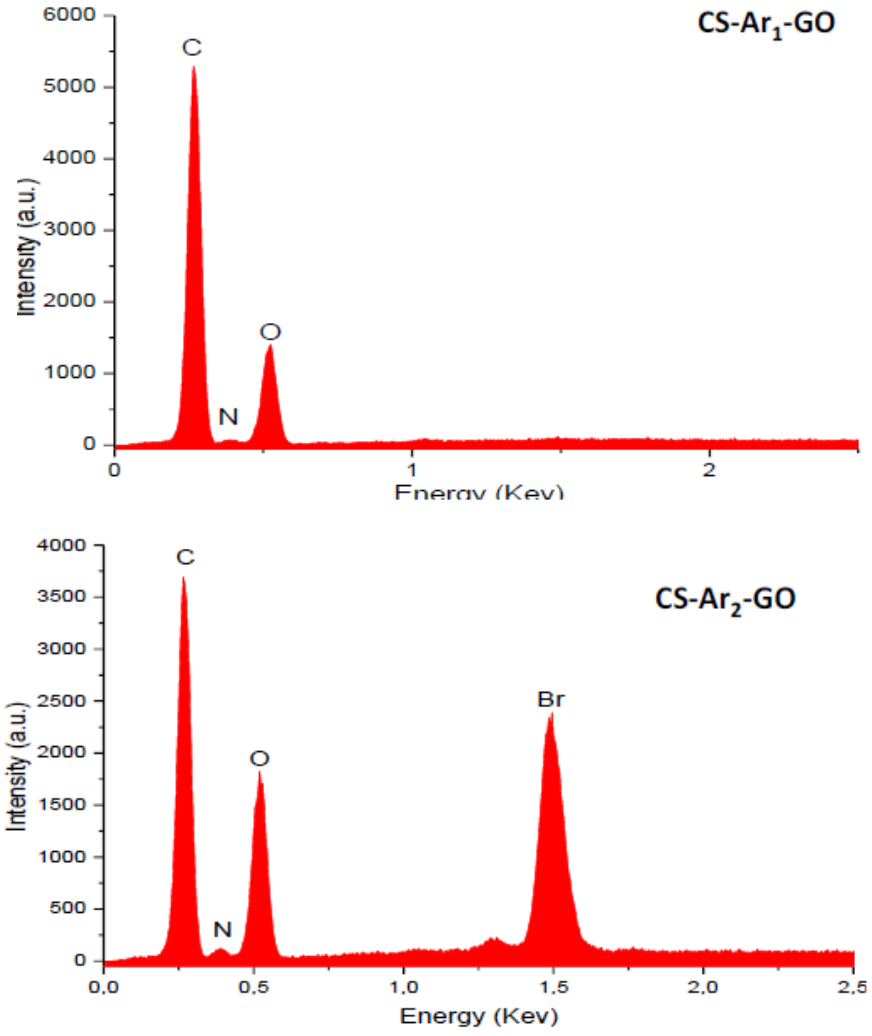

Published in : Carbohydrate Polymers (2020), vol.230, pp. 115634
DOI: 10.1016/j.carbpol.2019.115634
Status : Postprint (Author's version)

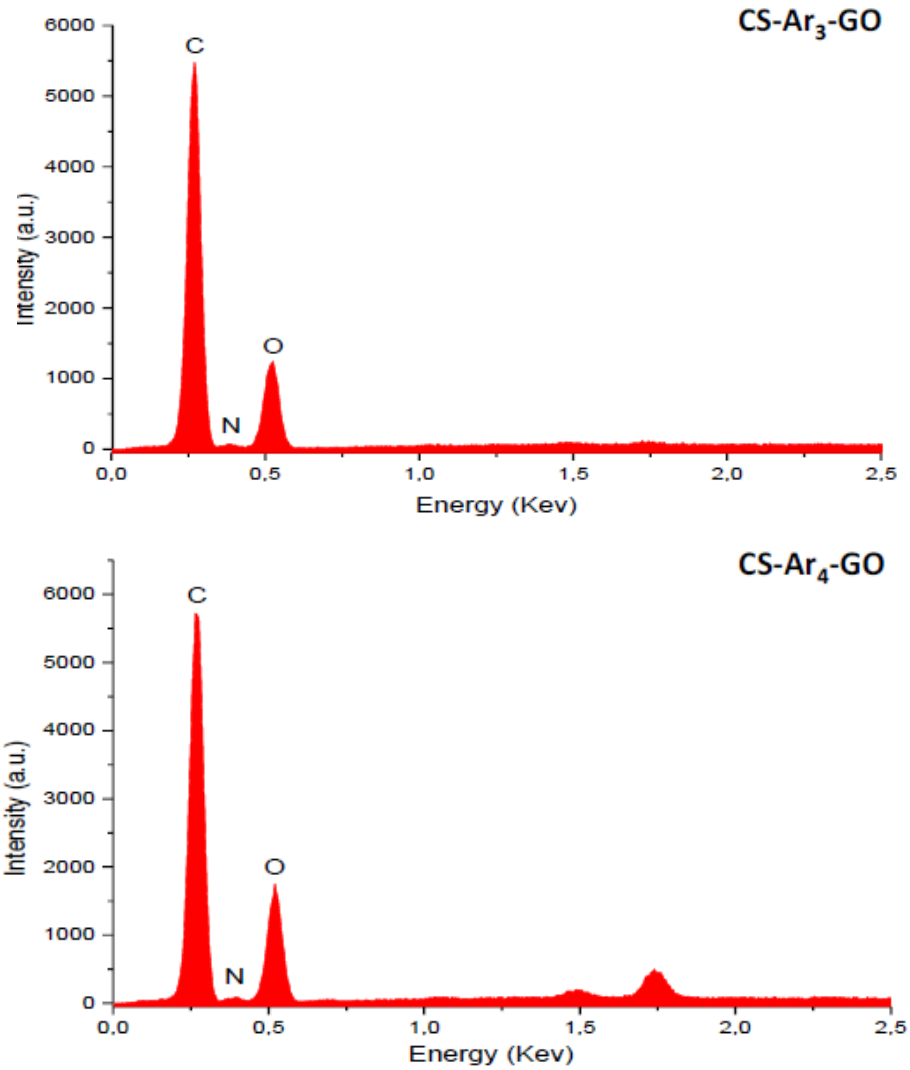

Published in : Carbohydrate Polymers (2020), vol.230, pp. 115634
DOI: 10.1016/j.carbpol.2019.115634
Status : Postprint (Author's version)

Figure S6: Thermal behavior of **CS-Ar$_x$-*f***.by TGA and DSC :

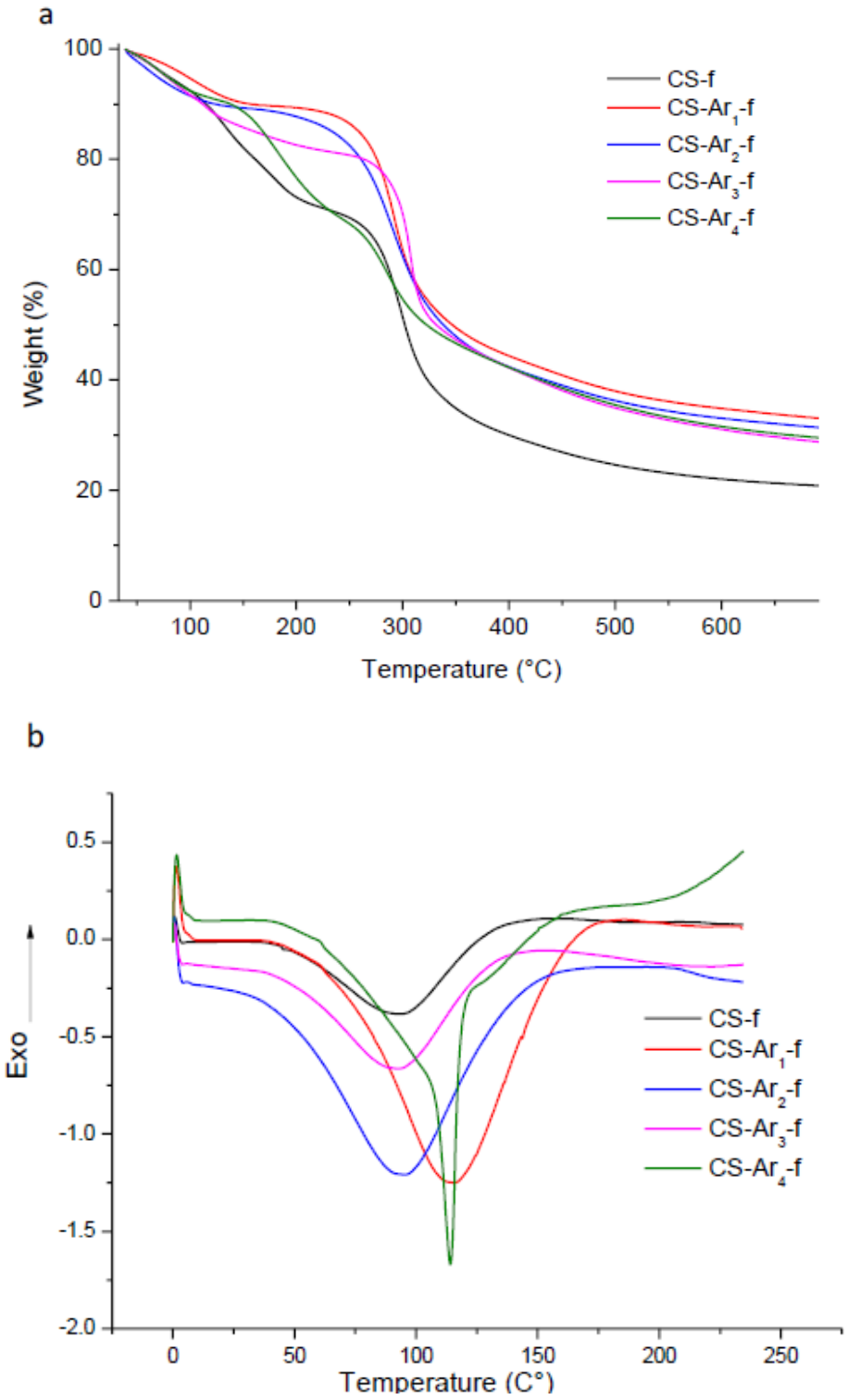

Published in : Carbohydrate Polymers (2020), vol.230, pp. 115634
DOI: 10.1016/j.carbpol.2019.115634
Status : Postprint (Author's version)

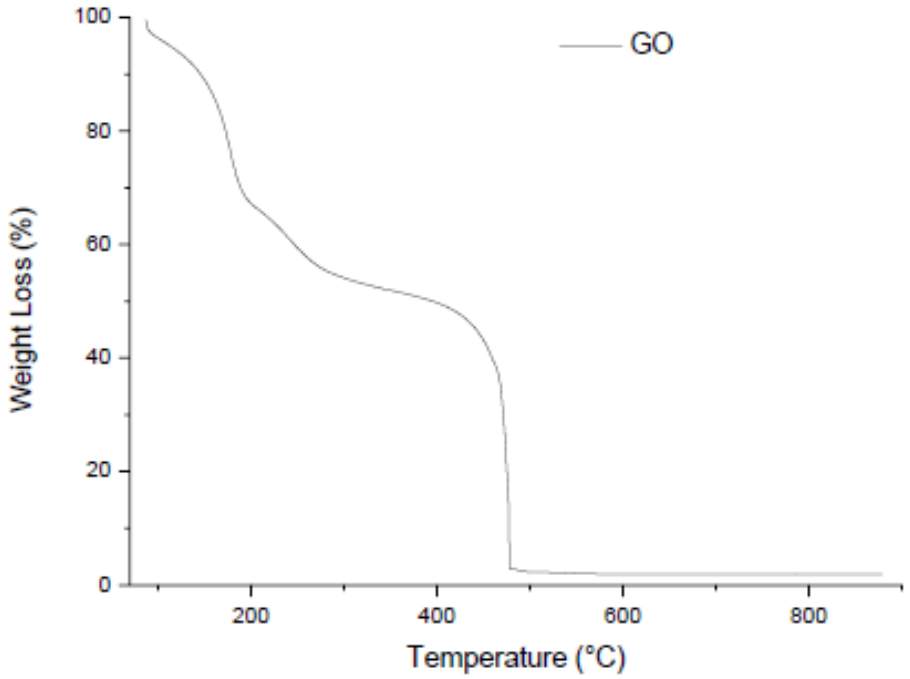

Figure S7: Stress–strain curves of **CS-f**, **CS-Arx-*f***, **CS-GO-*f*** and **CS-Arx-GO-*f*** :

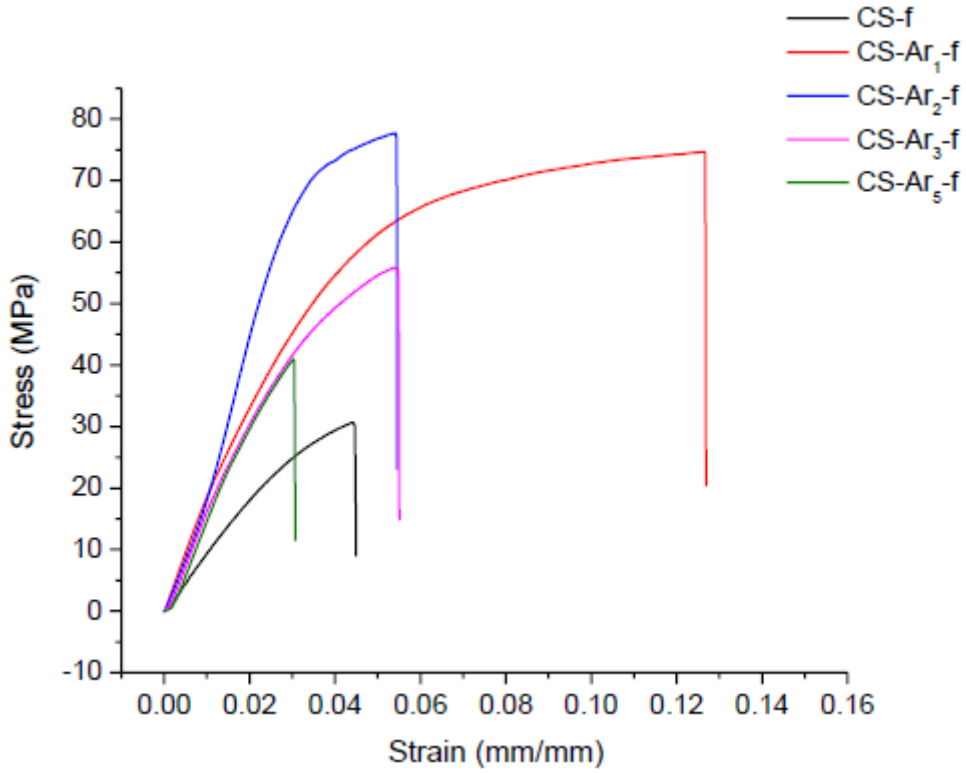

Published in : Carbohydrate Polymers (2020), vol.230, pp. 115634
DOI: 10.1016/j.carbpol.2019.115634
Status : Postprint (Author's version)

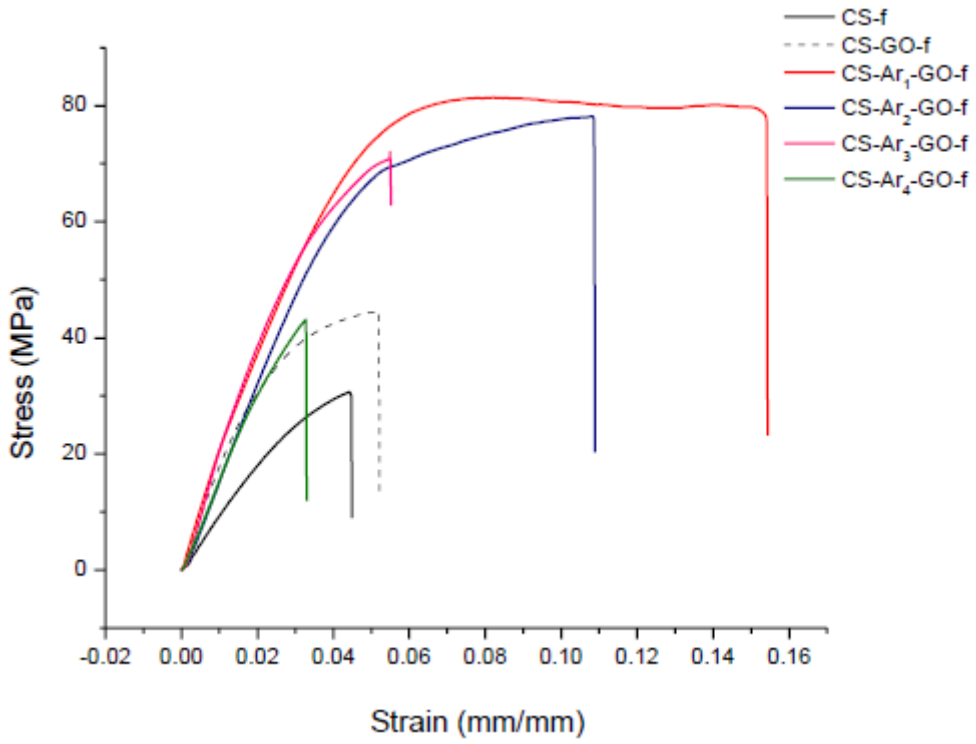

Figure S8: Temperature-dependence aldehyde release from **CS-Arx-*f*** and **CS-Arx-GO-*f*** :

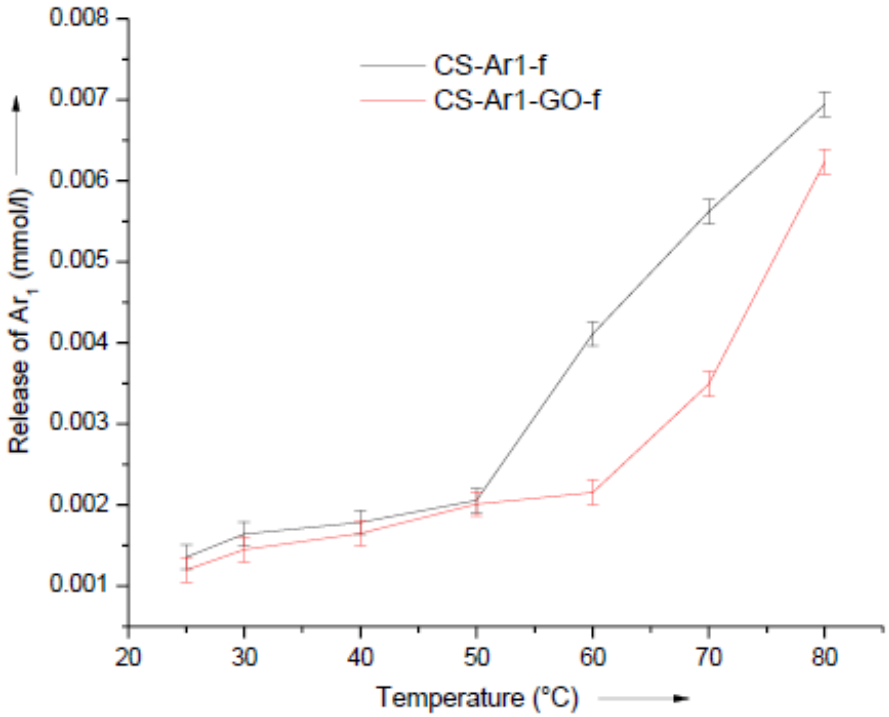

Published in : Carbohydrate Polymers (2020), vol.230, pp. 115634
DOI: 10.1016/j.carbpol.2019.115634
Status : Postprint (Author's version)

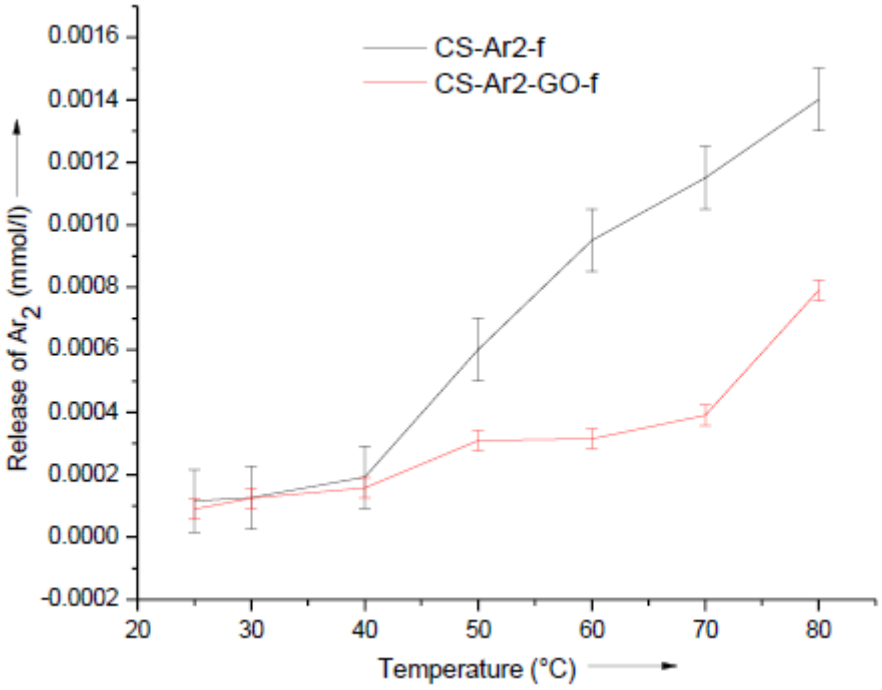

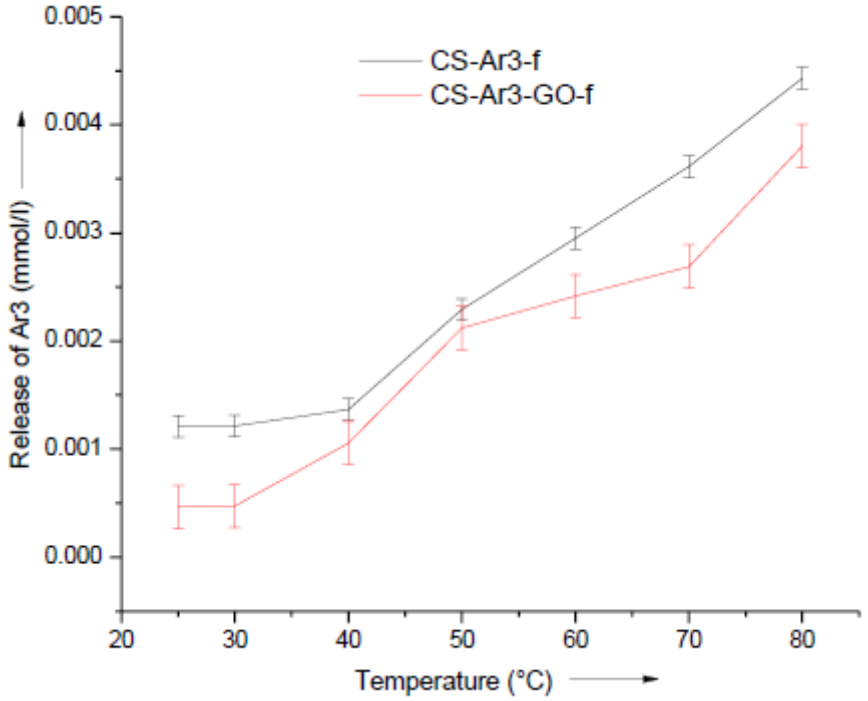

Published in : Carbohydrate Polymers (2020), vol.230, pp. 115634
DOI: 10.1016/j.carbpol.2019.115634
Status : Postprint (Author's version)

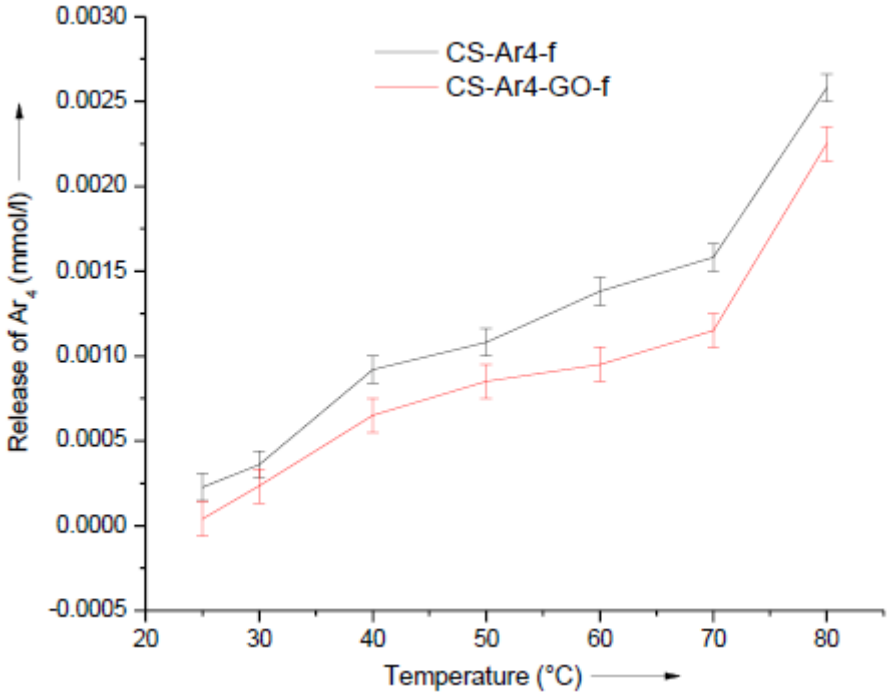

Figure S9: pH-dependence aldehyde release from **CS-Arx-*f*** and **CS-Arx-GO-*f*** :

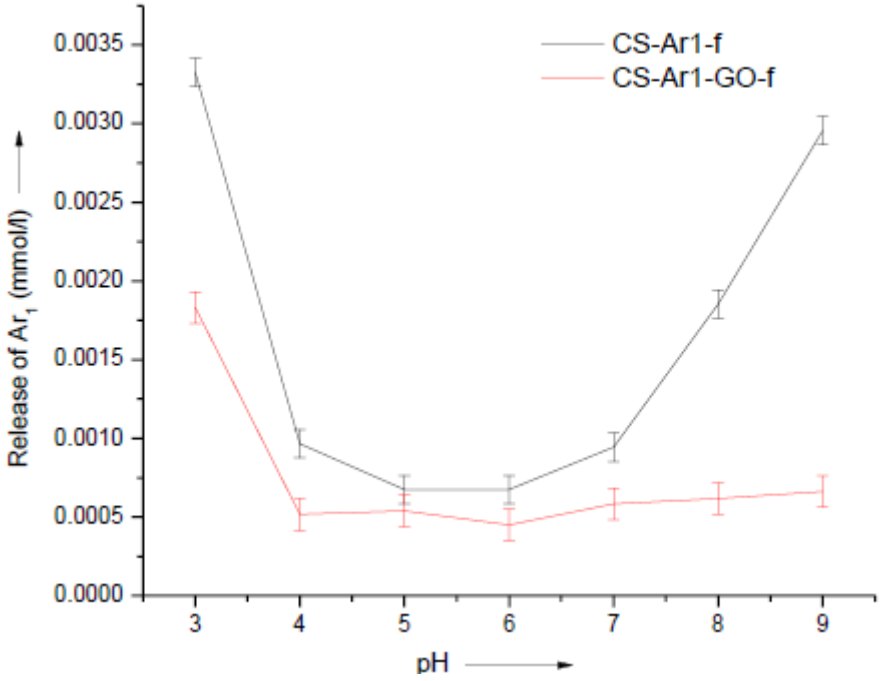

Published in : Carbohydrate Polymers (2020), vol.230, pp. 115634
DOI: 10.1016/j.carbpol.2019.115634
Status : Postprint (Author's version)

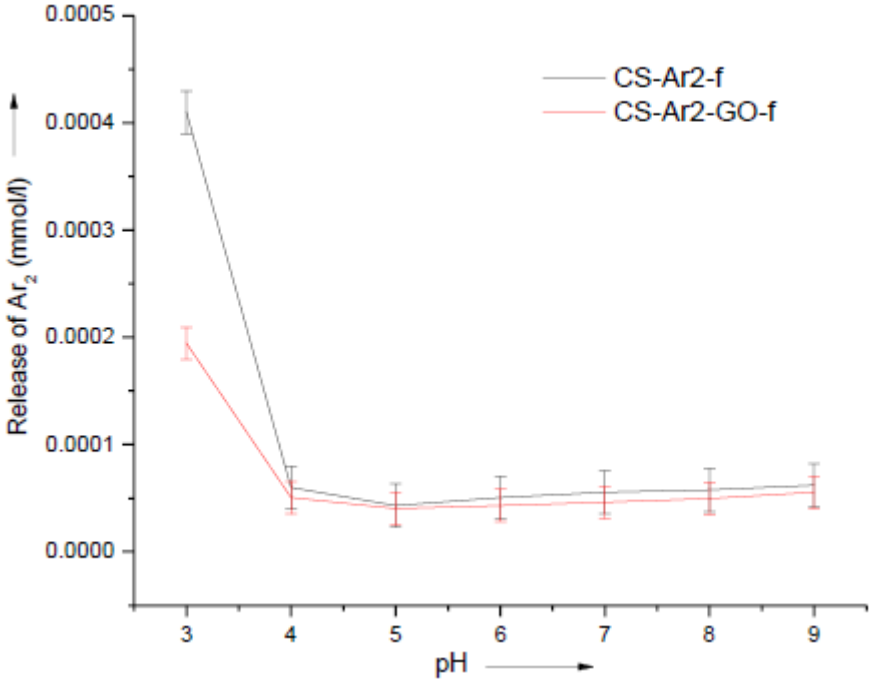

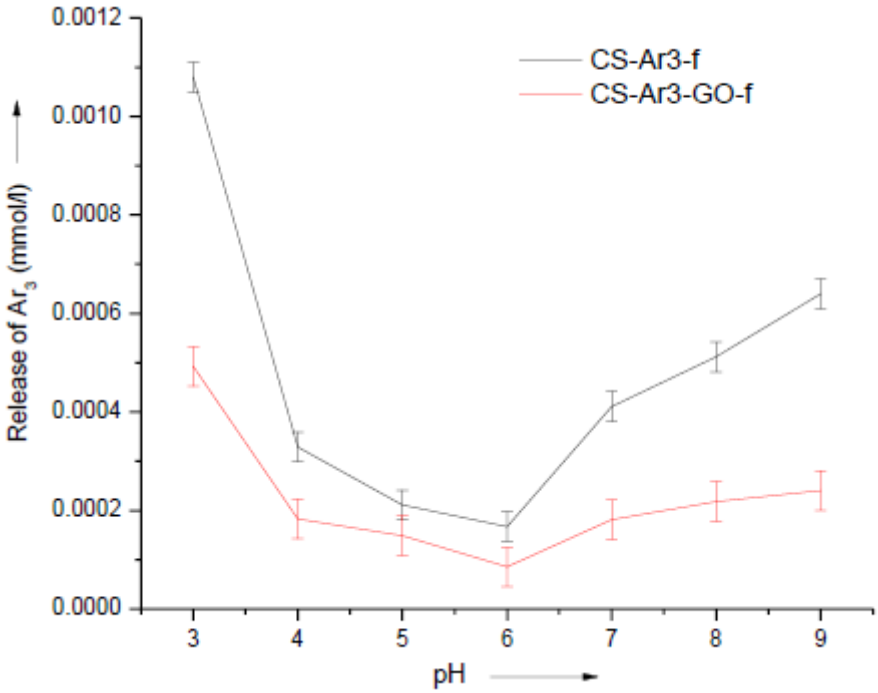

Published in : Carbohydrate Polymers (2020), vol.230, pp. 115634
DOI: 10.1016/j.carbpol.2019.115634
Status : Postprint (Author's version)

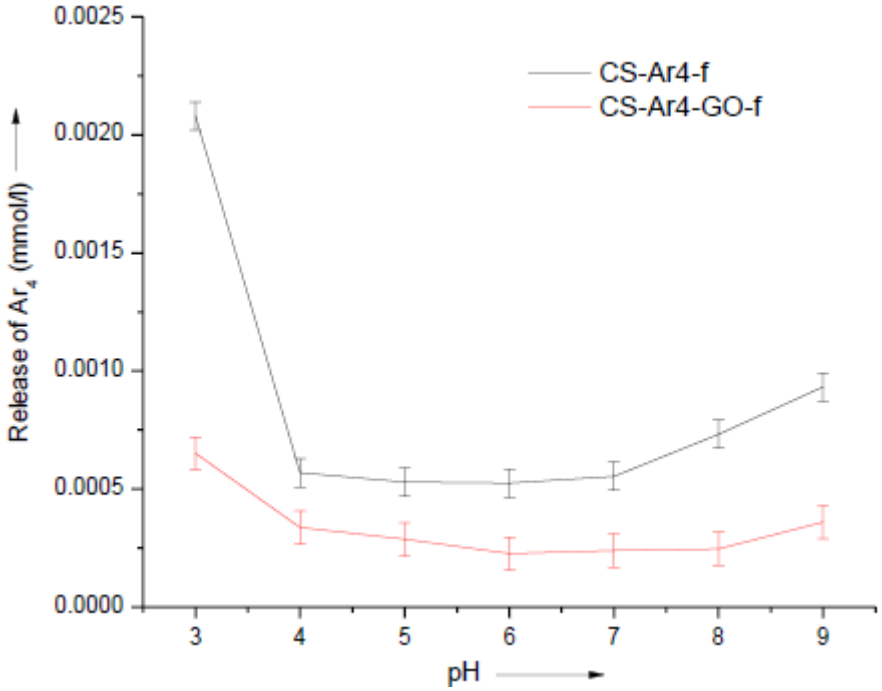

Figure S10: pH-dependence aldehyde release from **CS-Arx-*f*** and **CS-Arx-GO-*f*** :

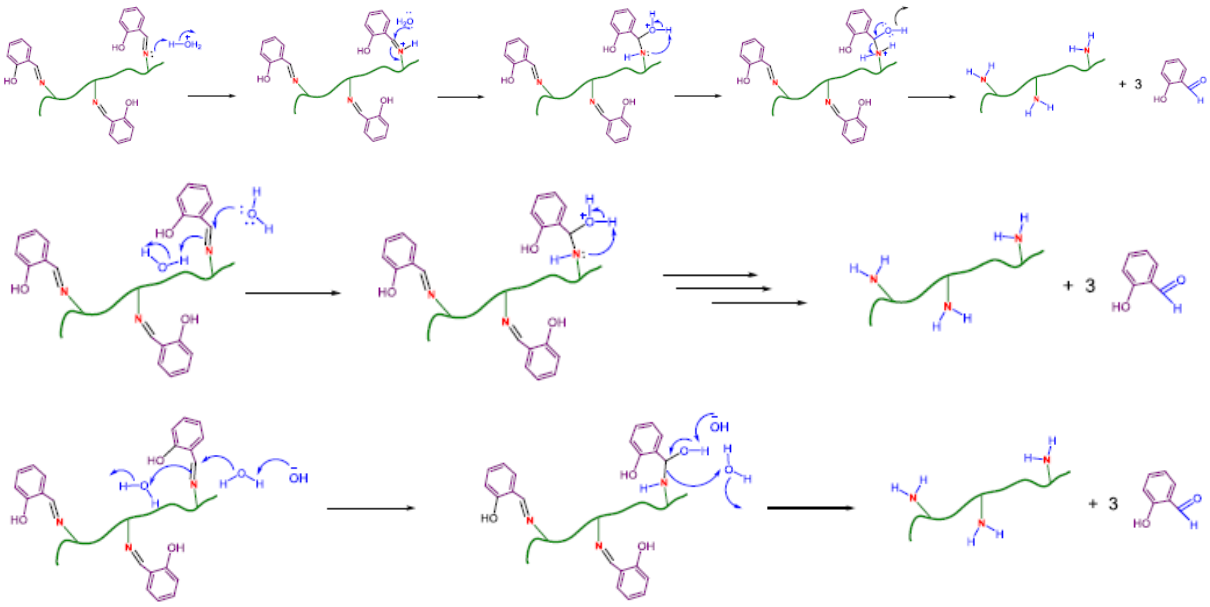

Published in : Carbohydrate Polymers (2020), vol.230, pp. 115634
DOI: 10.1016/j.carbpol.2019.115634
Status : Postprint (Author's version)

References

Ailincai, D., Bejan, A., Titorencu, I., Drobota, M., & Simionescu, B. C. (2014). Iminochitosan derivatives. Synthetic pathway and properties. Revue Roumaine Du Chimie, 59(6–7), 385–392.

Ailincai, D., Marin, L., Morariu, S., Mares, M., Bostanaru, A.-C., Pinteala, M., ... Barboiu, M. (2016). Dual crosslinked iminoboronate-chitosan hydrogels with strong antifungal activity against Candida planktonic yeasts and biofilms. Carbohydrate Polymers, 152, 306–316.

Alcântara, A. C. S., Darder, M., Aranda, P., & Ruiz-Hitzky, E. (2014). Polysaccharide–fibrous clay bionanocomposites. Applied Clay Science, 96, 2–8.

Anouar, A., Katir, N., Mamede, A.-S., Aboulaich, A., Draoui, K., Royer, S., & El Kadib, A. (2019). Synthesis and multifaceted use of phosphorylated graphene oxide: Growth of titanium dioxide clusters, interplay with gold nanoparticles and exfoliated sheets in bioplastics. Materials Chemistry Frontiers, 3, 242–250.

Antony, R., Arun, T., & Manickam, S. T. D. (2019). A review on applications of chitosanbased Schiff bases. International Journal of Biological Macromolecules, 129, 615–633.

Cervera, M. F., Heinämäki, J., Krogars, K., Jörgensen, A. C., Karjalainen, M., Colarte, A. I., & Yliruusi, J. (2004). Solid-state and mechanical properties of aqueous chitosanamylose starch films plasticized with polyols. AAPS Pharmacology Science Technology, 5(1), 109.

Chabbi, J., Jennah, O., Katir, N., Lahcini, M., Bousmina, M., & El Kadib, A. (2018). Aldehyde-functionalized chitosan-montmorillonite films as dynamically-assembled, switchable-chemical release bioplastics. Carbohydrate Polymers, 183, 287–293.

Croisier, F., & Jérôme, C. (2013). Chitosan-based biomaterials for tissue engineering. European Polymer Journal, 49(4), 780–792.

Crouvisier-Urion, K., Regina da Silva Farias, F., Arunatat, S., Griffin, D., Gerometta, M., Rocca-Smith, J. R., & Karbowiak, T. (2019). Functionalization of chitosan with lignin to produce active materials by waste valorization. Green Chemistry, 21(17), 4633–4641.

Darder, M., Colilla, M., & Ruiz-Hitzky, E. (2003). Biopolymer−Clay nanocomposites based on chitosan intercalated in Montmorillonite. Chemistry of Materials, 15(20), 3774–3780.

Darder, M., López-Blanco, M., Aranda, P., Aznar, A. J., Bravo, J., & Ruiz-Hitzky, E. (2006). Microfibrous chitosan−Sepiolite nanocomposites. Chemistry of Materials, 18(6), 1602–1610.

Dinu, M. V., Cocarta, A. I., & Dragan, E. S. (2016). Synthesis, characterization and drug release properties of 3D chitosan/clinoptilolite biocomposite cryogels. Carbohydrate Polymers, 153, 203–211.

Dohno, C., Okamoto, A., & Saito, I. (2005). Stable, specific, and reversible base pairing via schiff base. Journal of the American Chemical Society, 127(47), 16681–16684.

dos Santos, J. E., Dockal, E. R., & Cavalheiro, É. T. G. (2005). Synthesis and characterization of Schiff bases from chitosan and salicylaldehyde derivatives. Carbohydrate Polymers, 60(3), 277–282.

El Kadib, A. (2015). Chitosan as a sustainable organocatalyst: A concise overview. ChemSusChem, 8(2), 217–244.

El Kadib, A., & Bousmina, M. (2012). Chitosan bio-based organic–Inorganic hybrid aerogel microspheres. Chemistry - A European Journal, 18(27), 8264–8277.

El Kadib, A., Bousmina, M., & Brunel, D. (2014). Recent progress in chitosan bio-based Soft nanomaterials. Journal of Nanoscience and Nanotechnology, 14(1), 308–331.

Ennajih, H., Bouhfid, R., Essassi, E. M., Bousmina, M., & El Kadib, A. (2012). Chitosan–montmorillonite bio-based aerogel hybrid microspheres. Microporous and Mesoporous Materials, 152, 208–213.

Frindy, S., Primo, A., Qaiss, A., Bouhfid, R., Lahcini, M., Garcia, H., ... El Kadib, A. (2016). Insightful understanding of the role of clay topology on the stability of biomimetic hybrid chitosan-clay thin films and CO_2-dried porous aerogel microspheres. Carbohydrate Polymers, 146, 353–361.

Frindy, S., Primo, A., Ennajih, H., el kacem Qaiss, A., Bouhfid, R., Lahcini, M., & El Kadib, A. (2017). Chitosan–Graphene oxide films and CO_2-dried porous aerogel microspheres: Interfacial interplay and stability. Carbohydrate Polymers, 167, 297–305.

Garg, B., Bisht, T., & Ling, Y.-C. (2014). Graphene-based nanomaterials as heterogenous acid catalyst: A comprensive perspective. Molecules, 19(9), 14582–14614.

Godoy-Alcántar, C., Yatsimirsky, A. K., & Lehn, J.-M. (2005). Structure-stability correlations for imine formation in aqueous solution. Journal of Physical Organic Chemistry, 18(10), 979–985.

Hammi, N., Wrońska, N., Katir, N., Lisowska, K., Marcotte, N., Cacciaguerra, T., & El Kadib, A. (2019). Supramolecular chemistry-driven preparation of Nanostructured, transformable, and biologically active chitosan-clustered single, binary, and ternary metal oxide bioplastics. ACS Appl. Bio. Mater. 2(1), 61–69.

Han, D., Yan, L., Chen, W., & Li, W. (2011). Preparation of chitosan/graphene oxide composite film with enhanced mechanical strength in the wet state. Carbohydrate Polymers, 83(2), 653–658.

He, L., Wang, H., Xia, G., Sun, J., & Song, R. (2014). Chitosan/graphene oxide nanocomposite films with enhanced interfacial interaction and their electrochemical applications. Applied Surface Science, 314, 510–515.

Hong, P.-Z., Li, S.-D., Ou, C.-Y., Li, C.-P., Yang, L., & Zhang, C.-H. (2007). Thermogravimetric analysis of chitosan. Journal of Applied Polymer Science Applied Polymer Symposium, 105(2), 547–551.

Hsu, B. B., Jamieson, K. S., Hagerman, S. R., Holler, E., Ljubimova, J. Y., & Hammond, P. T. (2014). Ordered and kinetically discrete sequential protein release from biodegradable thin films. Angewandte Chemistry, 126(31), 8231–8236.

Hummers, W. S., & Offeman, R. E. (1958). Preparation of graphitic oxide. Journal of the American Chemical Society, 80(6), 1339.

Iftime, M.-M., Morariu, S., & Marin, L. (2017). Salicyl-imine-chitosan hydrogels: Supramolecular architecturing as a crosslinking method toward multifunctional hydrogels. Carbohydrate Polymers, 165, 39–50.

Jia, J., Gai, Y., Wang, W., & Zhao, Y. (2016). Green synthesis of biocompatiable chitosan–graphene oxide hybrid nanosheet by ultrasonication method. Ultrasonics Sonochemistry, 32, 300–306.

Jović-Jovičić, N., Mojović, Z., Darder, M., Aranda, P., Ruiz-Hitzky, E., Banković, P., ... Milutinović-Nikolić, A. (2016). Smectite-chitosan-based electrodes in electrochemical detection of phenol and its derivatives. Applied Clay Science, 124–125, 62–68.

Katir, N., Benayad, A., Rouchon, D., Marcotte, N., El Brahmi, N., Majoral, J. P., & El Kadib, A. (2019). Interfacial complexation driven three-dimensional assembly of cationic phosphorus dendrimers and graphene oxide sheets. Nanoscale Adv. 1, 314–321.

Ladet, S., David, L., & Domard, A. (2008). Multi-membrane hydrogels. Nature, 452, 76.

Macquarrie, D. J., & Hardy, J. J. E. (2005). Applications of functionalized chitosan in catalysis. Industrial & Engineering Chemistry Research, 44(23), 8499–8520.

Mahmoudi, N., Ostadhossein, F., & Simchi, A. (2016). Physicochemical and antibacterial properties of chitosan-polyvinylpyrrolidone films containing self-organized graphene oxide nanolayers. Journal of Applied Polymer Science, 133(11).

Marin, L., Simionescu, B., & Barboiu, M. (2012). Imino-chitosan biodynamers. Chemical Communications, 48(70), 8778–8780.

Marin, L., Stoica, I., Mares, M., Dinu, V., Simionescu, B. C., & Barboiu, M. (2013). Antifungal vanillin–imino-chitosan biodynameric films. Journal of Materials Chemistry B, 1(27), 3353–3358.

Marin, L., Moraru, S., Popescu, M.-C., Nicolescu, A., Zgardan, C., Simionescu, B. C., & Barboiu, M. (2014). Out-of-Water constitutional self-organization of chitosan–Cinnamaldehyde dynagels. Chemistry - A European Journal, 20(16), 4814–4821.

Marin, L., Ailincai, D., Mares, M., Paslaru, E., Cristea, M., Nica, V., & Simionescu, B. C. (2015). Imino-chitosan biopolymeric films. Obtaining, self-assembling, surface and antimicrobial properties. Carbohydrate Polymers, 117, 762–770.

Marin, L., Ailincai, D., Morariu, S., & Tartau-Mititelu, L. (2017). Development of biocompatible glycodynameric hydrogels joining two natural motifs by dynamic constitutional chemistry. Carbohydrate Polymers, 170, 60–71.

Mohammadi, Z., Mesgar, A. S.-M., & Rasouli-Disfani, F. (2016). Reinforcement of freezedried chitosan scaffolds with multiphasic calcium phosphate short fibers. Journal of the Mechanical Behavior of Biomedical Materials, 61, 590–599.

Published in : Carbohydrate Polymers (2020), vol.230, pp. 115634
DOI: 10.1016/j.carbpol.2019.115634
Status : Postprint (Author's version)

Nunthanid, J., Puttipipatkhachorn, S., Yamamoto, K., & Peck, G. E. (2001). Physical properties and molecular behavior of chitosan films. Drug Development and Industrial Pharmacy, 27(2), 143–157.
Olaru, A.-M., Marin, L., Morariu, S., Pricope, G., Pinteala, M., & Tartau-Mititelu, L. (2018). Biocompatible chitosan based hydrogels for potential application in local tumour therapy. Carbohydrate Polymers, 179, 59–70.
Ordikhani, F., Ramezani Farani, M., Dehghani, M., Tamjid, E., & Simchi, A. (2015). Physicochemical and biological properties of electrodeposited graphene oxide/chitosan films with drug-eluting capacity. Carbon, 84, 91–102.
Pan, Y., Wu, T., Bao, H., & Li, L. (2011). Green fabrication of chitosan films reinforced with parallel aligned graphene oxide. Carbohydrate Polymers, 83(4), 1908–1915.
Pavinatto, F. J., Caseli, L., & Oliveira, O. N. (2010). Chitosan in nanostructured thin films. Biomacromolecules, 11(8), 1897–1908.
Purwanto, M., Atmaja, L., Mohamed, M. A., Salleh, M. T., Jaafar, J., Ismail, A. F., & Widiastuti, N. (2016). Biopolymer-based electrolyte membranes from chitosan incorporated with montmorillonite-crosslinked GPTMS for direct methanol fuel cells. RSC Advances, 6(3), 2314–2322.
Rabea, E. I., Badawy, M. E. T., Stevens, C. V., Smagghe, G., & Steurbaut, W. (2003). Chitosan as antimicrobial agent: Applications and mode of action. Biomacromolecules, 4(6), 1457–1465.
Rinaudo, M. (2006). Chitin and chitosan: Properties and applications. Progress in Polymer Science, 31(7), 603–632.
Sahariah, P., & Másson, M. (2017). Antimicrobial chitosan and chitosan derivatives: A review of the structure–Activity relationship. Biomacromolecules, 18(11), 3846–3868.
Schiff, H. (1864). Mittheilungen aus dem Universitätslaboratorium in Pisa: Eine neue reihe organischer Basen. Justus Liebigs Annalen Der Chemie, 131(1), 118–119.
Song, J., Wang, X., & Chang, C.-T. (2014). Preparation and characterization of graphene oxide. J. Nanomater. 2014, 6.
Stroescu, M., Stoica-Guzun, A., Isopencu, G., Jinga, S. I., Parvulescu, O., Dobre, T., & Vasilescu, M. (2015). Chitosan-vanillin composites with antimicrobial properties. Food Hydrocolloids, 48, 62–71.
Suginta, W., Khunkaewla, P., & Schulte, A. (2013). Electrochemical biosensor applications of polysaccharides chitin and chitosan. Chemical Reviews, 113(7), 5458–5479.
Thakur, V. K., & Thakur, M. K. (2014). Recent advances in graft copolymerization and applications of chitosan: A review. ACS Sustainable Chem. Eng. 2(12), 2637–2652.
Tirkistani, F. A. A. (1998). Thermal analysis of some chitosan Schiff bases. Polymer Degradation and Stability, 60(1), 67–70.
Valentin, R., Bonelli, B., Garrone, E., Di Renzo, F., & Quignard, F. (2007). Accessibility of the functional groups of chitosan aerogel probed by FT-IR-Monitored deuteration. Biomacromolecules, 8(11), 3646–3650.
Wang, H., Qian, J., & Ding, F. (2018). Emerging chitosan-based films for food packaging applications. Journal of Agricultural and Food Chemistry, 66(2), 395–413.
Wu, Q., Liang, D., Ma, X., Lu, S., & Xiang, Y. (2019). Chitosan-based activated carbon as economic and efficient sustainable material for capacitive deionization of low salinity water. RSC Advances, 9, 26676–26684.
Yadav, M., & Ahmad, S. (2015). Montmorillonite/graphene oxide/chitosan composite: Synthesis, characterization and properties. International Journal of Biological Macromolecules, 79, 923–933.
Yadav, S. K., Jung, Y. C., Kim, J. H., Ko, Y.-I., Ryu, H. J., Yadav, M. K., ... Cho, J. W. (2013). Mechanically robust, electrically conductive biocomposite films using antimicrobial chitosan-functionalized graphenes. Particle & Particle Systems, 30(8), 721–727.
Yang, X., Tu, Y., Li, L., Shang, S., & Tao, X.-m. (2010). Well-dispersed Chitosan/Graphene oxide nanocomposites. ACS Applied Materials & Interfaces, 2(6), 1707–1713.
Yi, H., Wu, L.-Q., Bentley, W. E., Ghodssi, R., Rubloff, G. W., Culver, J. N., & Payne, G. F. (2005). Biofabrication with chitosan. Biomacromolecules, 6(6), 2881–2894.
Yuan, B., Bao, C., Qian, X., Song, L., Tai, Q., Liew, K. M., & Hu, Y. (2014). Design of artificial nacre-like hybrid films as shielding to mitigate electromagnetic pollution. Carbon, 75, 178–189.